

1 Interneuronal mechanisms of hippocampal theta oscillations in 2 full-scale models of the CA1 circuit

3 Marianne J. Bezaire^{2#}, Ivan Raikov^{1,2}, Kelly Burk², Dhruvil Vyas², and Ivan Soltesz¹

4 ¹Department of Neurosurgery, Stanford University, Stanford, CA 94305

5 ²Department of Anatomy and Neurobiology, University of California, Irvine, CA 92697

6 #Present address: Department of Psychological and Brain Sciences, Boston University, Boston, MA 02215

7 **Key words:** Network, model, oscillation, diversity, theta, inhibition, hippocampus

8 Correspondence

9 Marianne Bezaire, PhD

10 Email: marianne.bezaire@gmail.com

11 Abstract

12 The hippocampal theta rhythm plays important roles in information processing; however, the
13 mechanisms of its generation are not well understood. We developed a data-driven, supercomputer-
14 based, full-scale (1:1) model of the CA1 area and studied its interneurons during theta oscillations.
15 Theta rhythm with phase-locked gamma oscillations and phase-preferential discharges of distinct in-
16 terneuronal types spontaneously emerged from the isolated CA1 circuit without rhythmic inputs.
17 Perturbation experiments identified parvalbumin-expressing interneurons and neurogliaform cells, as
18 well as interneuronal diversity itself, as important factors in theta generation. These simulations reveal
19 new insights into the spatiotemporal organization of the CA1 circuit during theta oscillations.

Introduction

The hippocampal CA1 area supports diverse cognitive tasks including learning, memory, and spatial processing (Squire, 1992; Remondes and Schuman, 2004; Manns et al., 2007; Moser et al., 2008). These cognitive tasks are thought to require coordination of neuronal activity provided by physiological network oscillations, including the theta rhythm (Buzsáki, 2002; Buzsáki and Moser, 2013). In rodents, hippocampal theta is a 5-10 Hz oscillation in the local field potential (LFP) and neuronal firing probabilities (Soltesz and Deschenes, 1993; Lee et al., 1994; Ylinen et al., 1995; Klausberger and Somogyi, 2008; Varga et al., 2012, 2014), occurring during locomotion and in REM sleep (Buzsáki, 2002). Though several major afferents provide theta-frequency rhythmic input to the CA1 *in vivo* (Soltesz and Deschenes, 1993; Buzsáki, 2002; Fuhrmann et al., 2015), recent reports indicate the presence of spontaneous theta-frequency LFP oscillations even in the isolated whole CA1 preparation *in vitro* (Goutagny et al., 2009; Amilhon et al., 2015). Therefore, the latter studies suggest an intrinsic ability of the CA1 circuit to generate some form of theta waves even without rhythmic external inputs. However, the intra-CA1 mechanisms that may contribute to the generation of the theta rhythm are not well understood (Colgin, 2013, 2016).

Here we investigated the ability of the CA1 to generate intrinsic theta oscillations using a uniquely biological data-driven, full-scale computer model of the isolated CA1 network. Recent advances in supercomputing power and high-quality synaptic connectivity data present the intriguing opportunity to develop full-scale models where every biological synapse and neuron is explicitly represented. In principle, such full-scale models of mammalian circuits comprising hundreds of thousands of neurons of distinct types advantageously avoid the connectivity scaling tradeoff that besets reduced-scale models: smaller models of large networks with realistic single cell electrophysiological properties (e.g., input resistance and resting membrane potential) remain silent unless synaptic strengths or numbers are arbitrarily increased beyond the biologically relevant levels to compensate for fewer inputs to their model cells (e.g., Dyhrfjeld-Johnsen et al. (2007); Sterratt et al. (2011)). Biological relevance may also increase as other network components are modeled in greater detail. However, full-scale models

1 require considerable computational resources. Further, such detailed models have a large parameter
2 space which risks being sub-optimally constrained by neurobiological properties that are only partially
3 quantified (Sejnowski et al., 1988). Because the CA1 area is one of the most extensively studied brain
4 regions, there are abundant anatomical and electrophysiological data about its organization, making
5 it a logical choice for the development of a full-scale model. The CA1 area is also worth modeling at
6 full-scale because of the diverse cognitive tasks it supports. These tasks likely require the simultaneous
7 processing of thousands of incoming and outgoing signals, and full-scale network models, at least in
8 principle, have the potential to match this *in vivo* processing capacity.

9 In this paper, we describe the development of a full-scale CA1 computational network model of
10 unprecedented biological detail and its application to gain insights into the roles and temporal orga-
11 nization of CA1 interneurons during theta rhythm. The simulated full-scale CA1 circuit was able to
12 spontaneously generate theta waves as well as phase-locked gamma oscillations. Furthermore, distinct
13 interneuron types discharged at particular phases of theta, demonstrating that phase-preferential fir-
14 ing (Klausberger et al., 2003, 2004, 2005; Ferraguti et al., 2005; Jinno et al., 2007; Fuentealba et al.,
15 2008; Klausberger and Somogyi, 2008; Varga et al., 2012; Lapray et al., 2012; Katona et al., 2014;
16 Varga et al., 2014) originates in part within the CA1 network. Perturbation experiments revealed
17 that parvalbumin-expressing (PV+) interneurons, neurogliaform cells, connections between CA1 pyra-
18 midal cells, and interneuronal diversity were important for theta generation. These results provide
19 new mechanistic insights into the emergence of the theta rhythm from within the CA1 circuitry and
20 the role of interneurons in theta oscillations.

21 Results

22 Development of data-driven, full-scale model of the isolated CA1

23 Details of the full-scale model are described in the Methods, and the most important features are
24 illustrated in Figures 1 and 2 and summarized here. Briefly, CA1 model cells were evenly distributed

1 within their respective layers in a 3-dimensional prism with realistic dimensions for the rodent hip-
2 pocampal CA1 region (Figure 1A and 1B). The model network contained 338,740 cells (similar to the
3 biological CA1 in rats, including 311,500 pyramidal cells and 27,240 interneurons) (Figure 1D-1E and
4 Figure 1 - figure supplement 1). In addition, the network also incorporated 454,700 artificial stimu-
5 lating cells (spiking units with random, Poisson-distributed inter-spike intervals) to simulate afferents
6 to CA1; the cell type-specific distribution, dendritic position, amplitude and kinetics of the excitatory
7 input synapses were all experimentally constrained by afferent CA3 and entorhinal cortical data. Cell
8 type-specific connectivity data, including cell numbers (Figure 1D) and convergence and divergence
9 values (Figure 1E; Figure 1 - figure supplement 1 and Table 1) were taken without alteration from
10 our previously published, in-depth, quantitative assessment of the CA1 circuit (Bezaire and Soltesz,
11 2013). Anatomical constraints of the connectivity were implemented in the model by accounting for
12 the distribution of the axonal boutons as a function of longitudinal and transverse distance from the
13 presynaptic cell soma (Figure 1 - figure supplement 2). The afferent divergence and convergence onto
14 the cells were also anatomically patterned, maintaining the topographical arrangement seen experi-
15 mentally (Hongo et al., 2015), for a total of 5.19 billion synaptic connections in the model network.
16 In addition, the remaining parameters that could not be constrained by experimental data were docu-
17 mented, with the assumptions used to arrive at them explicitly listed in Table 2 of Bezaire and Soltesz
18 (2013) and additional parameter calculations described in the Supplementary Material Section 3 of the
19 present paper. To highlight the many constraints applied in the current work and address the uncon-
20 strained model parameters, we characterized all model components (constrained and unconstrained)
21 in experimental terms, comparing with experimental data where possible (Figure 2; Supplementary
22 Material). For a four second simulation, the full-scale model required 3-4 terabytes (TB) of RAM
23 and four hours of execution time on a supercomputer using ~3000 processors (or up to 12 hours for
24 simulations calculating a high-accuracy local field potential (LFP) analog). Additional details and
25 data about model performance are available in Table 2 and Bezaire et al. (2016).

26 An important set of constraints was the electrophysiology and other properties of individual cells
27 and synapses (Figure 2; Tables 3 and 4) that were based on experimental data. Briefly, our pyra-

1 midal cell model (Poolos et al., 2002) contained 200 compartments in a realistic morphology and six
2 fully characterized ion channel types with kinetics and densities based on anatomical location within
3 the cell (Figure 2A-2C). We included eight model interneuron types (Klausberger and Somogyi, 2008;
4 Soltesz, 2006; Armstrong and Soltesz, 2012): PV+ basket cells (these fast-spiking cells synapse on
5 the somata and proximal dendrites of CA1 pyramidal cells), cholecystokinin+ (CCK+) basket cells
6 (these regular-spiking cells also innervate the somata and proximal dendrites, but have properties
7 and functions distinct from the PV+ basket cells), bistratified cells (these PV+ and somatostatin+
8 (SOM+) fast-spiking cells innervate the basal and apical dendritic trees), axo-axonic cells (these PV+
9 fast-spiking cells exclusively synapse on the axon initial segments of pyramidal cells and are also
10 known as chandelier cells), Schaffer Collateral-Associated (SC-A) cells (these CCK+, regular-spiking
11 cells innervate dendrites in the stratum radiatum), oriens-lacunosum-moleculare (O-LM) cells (these
12 SOM+ cells project to the distal dendrites in the stratum lacunosum-moleculare though their somata
13 are located in the stratum oriens), neurogliaform cells (these cells have relatively small dendrites and a
14 dense axonal cloud, and they innervate distal dendrites in the stratum lacunosum-moleculare), and ivy
15 cells (these cells are similar to neurogliaform cells, but innervate proximal dendrites) (Figure 2D-2J).
16 Some interneurons in the model, as in the biological network, also innervated other interneurons (Table
17 1). For greater detail of model connectivity, including convergence per single cell, synaptic amplitude,
18 and other factors, see the Supplementary Material. These cell types collectively comprise the majority
19 (~70%) of known CA1 interneurons (Bezaire and Soltesz, 2013). The remaining 30% of the interneu-
20 rons were not included in the model due to paucity of quantitative data (Bezaire and Soltesz, 2013).
21 We differentiated the interneurons by their electrophysiological profiles, connectivity patterns, synaptic
22 properties, and anatomical abundance (Gulyas et al., 1991; Hajos and Mody, 1997; Maccaferri et al.,
23 2000; Megías et al., 2001; Lee et al., 2010; Krook-Magnuson et al., 2011; Bezaire and Soltesz, 2013;
24 Lee et al., 2014). The synaptic connections were implemented using double exponential mechanisms
25 to better fit experimental data on rise and decay time constants. We used experimental data to
26 constrain the synaptic kinetics, amplitudes, and locations on the postsynaptic cell (Figures 1E, 2K,
27 and 2L). We implemented the model in parallel NEURON (Carnevale and Hines, 2005) and executed

1 the simulations on several supercomputers. All model results, characterizations, and experimental
2 comparisons are publically available.

3 **Emergence of spontaneous theta and gamma oscillations in the full-** 4 **scale model in the absence of rhythmic external inputs**

5 First, we examined whether the well-constrained, biologically detailed, full-scale CA1 model could os-
6 cillate spontaneously within the physiological range. Based on reports of spontaneous theta-frequency
7 LFP oscillations in the isolated CA1 preparation ([Goutagny et al., 2009](#)), we expected a sufficiently
8 constrained CA1 model to generate spontaneous theta rhythm when given tonic, arrhythmic exci-
9 tation. We varied the magnitude of arrhythmic, tonic excitation to the network (by systematically
10 changing the mean spiking frequency of the artificial stimulating cells, see above) and identified exci-
11 tation levels where the network developed a stable, spontaneous theta rhythm (5-10 Hz; [Figures 3](#) and
12 [4](#)). The pyramidal cell spikes ([Figures 3C](#) and [3D](#)) exhibited peak power around the theta frequency
13 of 7.8 Hz ([Figure 4](#) and [Table 7](#)). Importantly, every measure of network activity showed theta os-
14 cillations, including the somatic intracellular membrane potential from individual cells ([Figure 3D](#)),
15 the spike times of individual cells and all cells collectively ([Figure 3C](#)), and aggregate measures such
16 as the spike density function ([Szűcs, 1998](#)) per cell type and the LFP analog ([Figures 3A](#) and [4](#); see
17 also [Figure 4 - figure supplement 1](#)). In all of these measures of network activity, theta was apparent
18 within one theta period of the simulation start. The theta oscillation was stable, maintaining a steady
19 power level throughout the duration of the oscillation ([Figure 4A](#)). To our knowledge, this is the first
20 strictly data-driven, full-scale computational network model of the CA1 that exhibits spontaneous
21 theta rhythm without rhythmic synaptic inputs.

22 In addition to theta rhythm, the model network displayed gamma oscillations (25-80 Hz; [Fig-](#)
23 [ures 3B](#) and [4D](#)), as expected based on *in vivo* data ([Soltesz and Deschenes, 1993](#); [Tort et al., 2009](#);
24 [Colgin and Moser, 2010](#)) and *in vitro* slice data showing 65-75 Hz gamma oscillations arising in re-
25 sponse to theta rhythmic network stimulation ([Butler et al., 2016](#)). The amplitude envelope of the

1 gamma oscillation was phase-locked to the theta rhythm (Figure 3A, 3B and 4C), as it is in the bio-
2 logical CA1, representing cross-frequency coupling (Soltesz and Deschenes, 1993; Bragin et al., 1995;
3 Buzsáki et al., 2003; Jensen and Colgin, 2007; Belluscio et al., 2012). The highest amplitude of the
4 gamma oscillations in the model was observed at the theta trough ($0^\circ/360^\circ$) in the pyramidal layer
5 LFP analog (Figure 4C). Because the current study focused primarily on theta oscillations and exper-
6 imental data from the isolated CA1 are available only for the theta rhythm (Goutagny et al., 2009;
7 Amilhon et al., 2015), the gamma oscillations were not examined further in the present study.

8 These results demonstrate that, in spite of gaps in our knowledge, our model was sufficiently well-
9 constrained by experimental data that it generated theta and gamma oscillations on its own, without
10 extrinsic rhythmic inputs or deliberate tuning of intrinsic parameters.

11 Although in this paper we generally refrained from deliberately compensating for missing param-
12 eters, it is of course possible to do so. For example, as mentioned above, no sufficiently detailed
13 information was available for certain interneuron types. Therefore, these lesser-known interneurons
14 were not included in the model, which meant that inhibition received by the pyramidal cells was
15 probably weaker than in the biological situation. Indeed, the pyramidal cells in our model described
16 above (Figures 3 and 4) tended to fire more than they typically do so during theta oscillations *in*
17 *vivo* (e.g., Soltesz and Deschenes (1993); Robbe et al. (2006)). Is the higher firing frequency of the
18 pyramidal cells related to the weaker inhibition? To answer to latter question, in a subset of the
19 simulations we artificially scaled up inhibition in the model to match the inhibitory synapse numbers
20 on CA1 pyramidal cells that were expected from electron microscopic reconstructions of pyramidal
21 cell dendrites and somata (Megías et al., 2001; Bezaire and Soltesz, 2013). The rationale for scaling
22 up inhibition in this way was that, as described in detail in Bezaire and Soltesz (2013), the estimates
23 of local inhibitory inputs to pyramidal cells were different when based on experimental observations
24 of presynaptic anatomy (local boutons available for synapsing from distinct types of intracellularly
25 filled and reconstructed interneurons) as opposed to postsynaptic anatomy (inhibitory post-synaptic
26 densities on pyramidal cell dendrites). In simulations with the model containing this rationally scaled
27 up inhibition, only 1% of the pyramidal cells were active, and they fired at a low rate of 1.8 Hz

1 (data not shown), closely resembling the *in vivo* condition (Soltesz and Deschenes, 1993; Robbe et al.,
2 2006). Therefore, the model was capable of reproducing the experimentally observed relatively low
3 firing frequencies for the principal cells during theta oscillations *in vivo*. However, because the source
4 of the additional inhibition onto CA1 principal cells has not yet been experimentally identified, we
5 used the connectivity estimates as constrained by experimental observations of axonal boutons and
6 lengths in the full scale model (without the scaled-up inhibition) described above (Figures 3 and 4)
7 in the subsequent computational experiments.

8 Mechanism of theta generation and phase-preferential firing of in- 9 terneurons in the full-scale model of the isolated CA1

10 Next, we examined the onset of the theta rhythm and the firing patterns of the various cell types
11 in the model circuit during theta oscillations (Figure 5 and Table 5). As mentioned above, distinct
12 interneuronal types, defined based on their selective axonal innervation patterns of the postsynaptic
13 domains of pyramidal cells, exhibit characteristic, cell-type-specific preferred phases of firing during
14 theta oscillations *in vivo* (Klausberger et al., 2003, 2004, 2005; Ferraguti et al., 2005; Jinno et al.,
15 2007; Fuentealba et al., 2008; Varga et al., 2012; Lapray et al., 2012; Katona et al., 2014; Varga et al.,
16 2014). Importantly, this fundamental property emerged spontaneously from the full-scale model,
17 without purposeful tuning of parameters except the mean spiking frequency and synaptic strength
18 of the artificial stimulating cells to set the incoming excitation levels from afferents (see Methods
19 for details). As expected, the numerically dominant pyramidal cells, whose intracellular membrane
20 potential oscillations to a large extent generate and underlie the extracellular LFP signal during theta
21 oscillations (Buzsáki et al., 2012), preferentially discharged around the trough $0^\circ/360^\circ$ of the LFP
22 analog theta rhythm (Figure 5A).

23 Interneurons in the model preferentially fired at specific phases of theta oscillations, depending
24 on the cell type. Their phase preferences fell into two broad categories (Figure 5A). The cells be-
25 longing to the first group, including the PV+ basket cells, bistratified cells and O-LM cells, were

1 most likely to fire at the theta trough compared to other theta phases. Since these cells received
2 substantial excitatory inputs from local CA1 pyramidal cells both in the biological state and in the
3 model (Bezaire and Soltesz, 2013), their firing in the isolated CA1 model was probably driven by the
4 pyramidal cell discharges around the theta trough. In contrast, the second group of cells, including
5 the ivy and neurogliaform cells, the CCK+ basket cells and the axo-axonic cells, fired least around
6 the theta trough, leading to an inverted firing probability distribution relative to the first group of
7 interneurons (Figure 5A). Their differing phase preferences were most likely due to a combination
8 of weak or non-existent excitatory inputs from local CA1 pyramidal cells and inhibition from the
9 interneurons that prominently discharged around the theta trough. In general agreement with the
10 first group of cells being strongly and rhythmically driven by the local pyramidal cells, there was a
11 correlation between the phase preference and the strength of modulation (Figure 5C; see Methods),
12 with the cells discharging around the trough all showing strong modulation of firing.

13 These results were in line with recent data from the isolated CA1 preparation *in vitro* (Ferguson et al.,
14 2015) which showed that cells belonging to the broadly defined SOM+ and PV+ classes (identified
15 using genetic drivers) displayed phase preferences similar to the O-LM, PV+ basket and bistratified
16 cells in our model (note that Ferguson and colleagues used LFP theta recorded in the stratum radia-
17 tum as reference, which is approximately 180 degrees out of phase with the pyramidal cell layer theta
18 used in this paper). In addition, the interneuronal phase preferences in the model were also remark-
19 ably similar to *in vivo* data from anesthetized animals (Figure 5B; because no data are available on
20 the phase preferential firing of morphologically identified interneurons from the isolated CA1 prepara-
21 tion, comparison is made here with results from anesthetized animals, from which the most complete
22 data sets are available; see also Discussion). Specifically, the majority (71%; 5/7) of the interneuron
23 types for which there were experimental data, including the CCK+ basket, axo-axonic, bistratified,
24 O-LM and neurogliaform cells, showed similar preferential maxima in their firing probabilities in the
25 model (Figure 5A) and *in vivo* (Figure 5B). The largest differences between the model and the *in vivo*
26 phase-preferential firing occurred for the PV+ basket cells and the ivy cells, suggesting that during
27 theta oscillations *in vivo* these cells may be strongly driven by CA3 afferents active during the late

1 falling phase of the theta cycle (Colgin and Moser, 2010); note that PV+ cells receive a high number
2 of excitatory inputs on their dendrites compared to other interneuron classes (Gulyas et al., 1999).
3 A comparison of the model and the anesthetized *in vivo* data is illustrated in Figure 5D, where the
4 arrows indicate the shift required for the model phase preferences (Figure 5A) to equal the *in vivo*
5 (Figure 5B) phase preferences; note that the required shifts (arrows) are small for all interneuron types
6 except PV+ basket and ivy cells. A clear majority of the interneuronal types in the model showed
7 phase preferences similar to the *in vivo* condition where rhythmically discharging afferent inputs are
8 present, indicating that theta-preferential discharges are to a large extent determined by the wiring
9 properties of the CA1 circuit itself.

10 **Perturbation experiments indicate a key role for interneuronal diver-** 11 **sity in the emergence of spontaneous theta**

12 Importantly, the ability to generate theta oscillations, phase-locked gamma oscillations, and theta-
13 related phase-preferential firing of distinct interneuronal subtypes was not a universal property of the
14 model. As shown in Figure 6A, our strongly constrained model only exhibited spontaneous theta
15 oscillations at certain levels of afferent excitation. The results described above (Figures 3-5) were
16 obtained with an afferent excitation level of 0.65 Hz (labeled as “Control” in Figure 6A), meaning
17 that each excitatory afferent cell excited the model network with a Poisson-distributed spike train
18 having a Poisson mean interspike interval (ISI) corresponding to a firing rate of 0.65 Hz. When the
19 excitation level decreased below 0.65 Hz, the theta rhythm fell apart, and when the excitation level
20 increased beyond 0.80 Hz, theta power also started to drop significantly as the oscillation frequency
21 rose out of theta range (Figure 6 and Figure 6 - figure supplement 1), evolving into a beta oscillation
22 (Engel and Fries, 2010). These data indicate that while synaptic-cellular organization of the CA1
23 circuit enables the intrinsic, within-CA1 generation of theta waves, the circuit is predisposed to exhibit
24 theta oscillations only under particular excitatory input conditions. The observation that, under
25 certain conditions the model network can oscillate at frequencies between 12 and 20 Hz, is in agreement

1 with recent experimental findings that rhythmic driving of septal PV+ cells can reliably entrain the
2 hippocampus in a 1:1 ratio up to frequencies of 20 Hz (Dannenberg et al., 2015).

3 Does the parameter sensitivity of the theta rhythm also apply to recurrent excitation from pyra-
4 midal cells and inhibition from CA1 interneurons? In order to answer the latter question, we tested
5 whether the theta rhythm was differentially sensitive to the contribution of each inhibitory cell type
6 (Figure 6B). We characterized the contribution of each local CA1 cell type to the theta rhythm by
7 muting the output of the cell type so that its activity had no effect on the network. First, we stud-
8 ied the role of the recurrent collaterals of pyramidal cells, which contact mostly interneurons and,
9 less frequently, other pyramidal cells (Bezaire and Soltesz, 2013). When we muted all the outputs
10 from pyramidal cells, theta rhythm disappeared (bar labeled “Pyr” in Figure 6B), indicating that the
11 recurrent collaterals of pyramidal cells play a key role in theta oscillations.

12 Interestingly, muting the relatively rare CA1 pyramidal cell to pyramidal cell excitatory connections
13 alone (each pyramidal cell contacts 197 other pyramidal cells in the CA1; Bezaire and Soltesz (2013))
14 was sufficient to collapse the theta rhythm (bar labeled “None” in Figure 6C); key roles for inter-
15 pyramidal cell excitatory synapses within CA1 have been suggested for sharp wave ripple oscillations
16 as well (Maier et al., 2011). Furthermore, the parameter-sensitivity of the theta rhythm was also
17 apparent when examining the role of pyramidal cell to pyramidal cell connections, because theta power
18 dramatically decreased when these connections were either increased (doubled) or decreased (halved)
19 from the biologically observed 197 (Figure 6C). Next, we investigated the effects of muting the output
20 from each interneuron type. Silencing the output from any of the fast-spiking, PV family interneurons
21 (PV+ basket, axo-axonic, or bistratified cells), CCK+ basket cells, or neurogliaform cells also strongly
22 reduced theta power in the network (Figure 6B). In contrast, muting other interneuronal types (S.C.-A
23 cells, O-LM cells, or ivy cells) had no effect on this form of theta oscillations generated by the intra-
24 CA1 network (Figure 6B). In additional disinhibition studies simulating optogenetic experimental
25 configurations, partial muting of all PV+ outputs (PV+ basket, bistratified, and axo-axonic cells
26 together) had a larger effect than partial muting of all SOM+ outputs (O-LM and bistratified cells);
27 see Figure 6D. Reassuringly, these results were in overall agreement with experimental data from the

1 isolated CA1 preparation indicating that optogenetic silencing of PV+ cells, but not SOM+ cells
2 such as the O-LM cells, caused a marked reduction in theta oscillations (Amilhon et al., 2015). The
3 differential effects of silencing PV+ versus SOM+ cells could also be obtained in a rationally simplified
4 model called the Network Clamp, where a single pyramidal cell was virtually extracted from the full-
5 scale CA1 network with all of its afferent synapses intact (for further details, see Bezaire et al. (2016)).

6 Since the diverse sources of inhibition from the various interneuronal types are believed to enable
7 networks to achieve more complex behaviors, including oscillations (Soltesz, 2006; Rotstein et al.,
8 2005; Kepecs and Fishell, 2014), we next tested if reducing the diversity of interneurons in the model
9 would affect its ability to produce spontaneous theta oscillations. Surprisingly, giving all interneurons
10 a single electrophysiological profile appeared to create conditions that were not conducive for the ap-
11 pearance of spontaneous theta oscillations regardless of which interneuronal profile was used (Figure
12 6E; note that the cells still differed in the strengths, distribution, and identities of their incoming
13 and outgoing connections after this manipulation). To probe this finding further, we focused on PV+
14 basket cells, which have been implicated in theta generation *in vivo* (Soltesz and Deschenes, 1993;
15 Buzsáki, 2002; Stark et al., 2013; Hu et al., 2014) and exhibited strong theta power in their spiking in
16 the control network model (Figure 4B). We gradually altered (“morphed”) the properties of all other
17 model interneuron types until they became PV+ basket cells, by first converging their electrophysio-
18 logical profiles, then additionally their synaptic kinetics and incoming synapse weights, then also their
19 incoming synapse numbers, and finally their outgoing synaptic weights and numbers (Figure 6F; Table
20 7). Theta was not apparent in any intermediate steps nor in the final network where all interneurons
21 had become PV+ basket cells (“All PV+B” in Figure 6F). Furthermore, introduction of cell to cell
22 variability in the resting membrane potential of interneurons in the “All PV+B” configuration at the
23 biologically observed values for PV+ basket cells also failed to restore theta (“Var PV+B” in Figure
24 6F shows results with standard deviation of (SD) = 8 mV in the resting membrane potential; SD = 9
25 mV and SD = 2 mV also yielded no theta; biological SD value: approximately 5 mV in Tricoire et al.
26 (2011) and 2 mV in Mercer et al. (2012)). Therefore, although PV basket cells appear to be important
27 for theta-generation both in the biological and the model CA1 network, endowing all interneurons with

1 PV basket cell-like properties does not lead to a network configuration conducive to theta oscillations
2 ([Hendrickson et al., 2015](#)).

3 To rule out the possibility that the lack of theta could be due to an inappropriate excitation level
4 in these reduced diversity configurations, we subjected the “All PV+ B” network to a wide range of
5 incoming excitation levels (Figure 6G). Theta rhythm did not appear at any of these excitation levels.
6 While we could not rule out a hypothetical theta regime somewhere in the parameter space of such
7 low-diversity configurations, any theta solution space would likely be smaller and more elusive than
8 we were able to determine in the control configuration (Figure 6A).

9 Taken together, these results indicated, for the first time, that interneuronal diversity itself is an
10 important factor in the emergence of spontaneous theta oscillations from the CA1 network.

11 Neurogliaform cell signaling and theta generation in the isolated CA1 12 model

13 In agreement with previous predictions ([Capogna, 2011](#)), the perturbation experiments described
14 above suggested that neurogliaform cells were a necessary component for spontaneous theta to arise
15 in the isolated CA1. We wondered why muting the output from neurogliaform cells, but not the closely
16 related ivy cells, affected theta oscillations (Figure 6B), especially since there were fewer neurogliaform
17 cells than ivy cells, and they were less theta modulated (Figure 5A). These two model interneuron
18 groups mainly differed in that the neurogliaform cells evoked mixed GABA_{A,B} postsynaptic events
19 ([Price et al., 2005](#)), whereas the model ivy cells only triggered GABA_A IPSPs (in agreement with
20 a lack of evidence for ivy cell-evoked GABA_B IPSPs). Could the slow kinetics of GABA_B IPSPs
21 contribute to the pacing of the theta oscillations? Indeed, when we selectively removed the GABA_B
22 component of all neurogliaform cell outgoing synaptic connections, theta power was strongly reduced
23 (Figure 6H). To test whether the contribution of the GABA_B receptors was due to their slow kinetics,
24 we artificially sped up the GABA_B IPSPs so that they had GABA_A kinetics but conserved their
25 characteristic large charge transfer. This alteration was implemented by scaling up the GABA_A

1 synaptic conductance at neurogliaform cell output synapses to achieve a similar total charge transfer
2 as the control GABA_{A,B} mixed synapse (Figure 6 - figure supplement 2). As shown in Figure 6H
3 (green bar), theta activity was restored when the neurogliaform cell output synapses had no slow
4 GABA_B component, only a scaled up fast GABA_A IPSP with a charge transfer equivalent to the
5 mixed GABA_{A,B} synapses. Therefore, muting the neurogliaform cells strongly disrupted the theta
6 oscillations not because the theta oscillations required the slow kinetics of GABA_B IPSPs specifically,
7 but because the slow kinetics enabled a large total charge transfer.

8 Discussion

9 Emergence of theta oscillations from a biological data-driven, full- 10 scale model of the CA1 network

11 We produced a biologically detailed, full-scale CA1 network model constrained by extensive experi-
12 mental data (Bezaire and Soltesz, 2013). When excited with arrhythmic inputs at physiologically rel-
13 evant levels (see below), the model displayed spontaneous theta (and gamma) oscillations with phase
14 preferential firing across the nine model cell types (pyramidal cells and eight interneuron classes).
15 Consistent with experimental results (Goutagny et al., 2009; Amilhon et al., 2015), these oscillations
16 emerged from the network model without explicit encoding, rhythmic inputs or purposeful tuning of
17 intra-CA1 parameters (all anatomical connectivity parameters were exactly as previously published
18 in Bezaire and Soltesz (2013)). Cell type-specific perturbations of the network showed that each in-
19 terneuronal type contributed uniquely to the spontaneous theta oscillation, and that the presence
20 of diverse inhibitory dynamics was a necessary condition for sustained theta oscillations. In addi-
21 tion to characterizing roles for specific network components, these model results generally suggest
22 that the presence of diverse interneuronal types and the intrinsic circuitry of the CA1 network are
23 sufficient and necessary to enable the isolated CA1 to oscillate at spontaneous theta rhythms while
24 supporting distinct phase preferences of each class of hippocampal neuron. These abilities may serve

1 to maintain the stability and robustness of the theta oscillation mechanism as it operates *in vivo*
2 in diverse behavioral states. The theta rhythm is thought to be important for organizing disparate
3 memory tasks (Lisman and Idiart, 1995; Hasselmo et al., 2002; Hasselmo, 2005; Lisman and Jensen,
4 2013; Siegle and Wilson, 2014), and a CA1 network which has evolved a predisposition to oscillate at
5 theta and gamma frequencies may enable more efficient processing of the phasic input it receives *in*
6 *vivo* (Akam and Kullmann, 2012; Fries, 2015). In turn, phase preferential firing may aid information
7 processing tasks by providing order and allowing multiple channels of information to be processed in
8 parallel (Jensen and Lisman, 2000; Hasselmo et al., 2002; Womelsdorf et al., 2007; Schomburg et al.,
9 2014; Jeewajee et al., 2014; Maris et al., 2016).

10 Importantly, theta oscillations appeared only within certain levels of excitatory afferent activ-
11 ity, around 0.65 Hz for the average firing rate of the Poisson-distributed spike trains. When the
12 454,700 stimulating afferents in the model (representing the CA3 and entorhinal synapses; calculated
13 in Bezaire and Soltesz (2013)) are active at a Poisson mean of 0.65 Hz, they generate approximately
14 37,900 incoming spikes / theta cycle, given a theta frequency of 7.8 Hz (Equation 1).

$$16 \quad 454,700 \text{ afferents} * \frac{0.65 \text{ spikes/s}}{7.8 \text{ theta cycles/s}} = 37,892 \text{ spikes/cycle} \quad (1)$$

17
18 Is the latter number of spikes in the afferents to the CA1 network within a physiologically plausible
19 range? The biological CA1 network receives most of its input from CA3 and entorhinal cortical layer
20 III (ECIII), and it has been estimated that about 4% of CA3 pyramidal cells fire up to four spikes
21 per theta wave (Gasparini and Magee, 2006). We previously estimated 204,700 pyramidal cells in
22 ipsilateral CA3 (Bezaire and Soltesz, 2013), giving an estimated 32,750 spikes from ipsilateral CA3
23 per theta cycle (Equation 2).

$$24 \quad 204,700 \text{ cells} * .04 \text{ cell fraction} * 4 \text{ spikes/cell} = 32,752 \text{ spikes} \quad (2)$$

25 About 250,000 principal cells from ipsilateral ECIII synapse onto the CA1 region (Andersen et al.,

1 2006), and approximately 2% of these cells are active per theta cycle at a low firing rate (Csicsvari et al.,
2 1999; Mizuseki et al., 2009). Therefore, ECIII cells could provide 5,000 input spikes to ipsilateral CA1
3 (Equation 3).

$$4 \quad 250,000 \text{ cells} * .02 \text{ cell fraction} * 1 \text{ spike/cell} = 5,000 \text{ spikes} \quad (3)$$

5 Therefore, about 37,750 spikes per theta cycle arrive from ipsilateral CA3 and entorhinal cortex to the
6 CA1 network *in vivo*, which is reassuringly close to the our modeling results indicating that robust
7 theta emerged when the CA1 network model received approximately 37,900 afferent spikes per theta
8 cycle. Thus, the model has the capacity to process a biologically realistic number of spike inputs per
9 cycle while maintaining the theta rhythm.

10 Our results obtained using the 0.65 Hz excitation indicated that the CA1 model network exhibited
11 phenomena that corresponded well with experimental results, for example, on the differential roles of
12 PV+ basket cells and OLM cells. In addition, the simulations unexpectedly revealed that interneuronal
13 diversity itself may also be important in theta generation, since conversion of all interneurons into
14 fast spiking PV+ basket cells did not result in a network that was conducive for the emergence of
15 theta, in spite of the key role of the PV+ basket cells in hippocampal oscillations. The modeling
16 results also provided the interesting insight that GABA_B receptors may play important roles in slow
17 oscillations such as the theta rhythm not because their slow kinetics pace the oscillations, but because
18 their slow kinetics enable a massive charge transfer. This insight was illuminated by the fact that
19 slow GABA_B synapses were not necessary for theta as long as their large charge was carried by the
20 fast GABA_A synapses. However, we had to increase the conductance of the GABA_A synapse almost
21 300 times to achieve a similar charge transfer as that conveyed by the GABA_B synapse. Such a large
22 conductance is not biologically realistic, indicating that the key role for GABA_B synapses may be
23 to allow the temporal distribution of the large synaptic charge transfer. Indeed, the importance of
24 GABA_B receptors has also been indicated by a number of recent experimental studies, for example,
25 in the modulation of theta and gamma oscillations (Kohl and Paulsen, 2010), setting of spike timing

1 of neuron types during theta (Kohl and Paulsen, 2010), and playing a role in cortical oscillations and
2 memory processes (Craig and McBain, 2014).

3 In addition to identifying key roles for certain inhibitory components (PV+ interneurons, neu-
4 rogliaform cells, GABA_B, and interneuron diversity), our results also highlighted the importance of
5 the recurrent excitatory collaterals from CA1 pyramidal cells in theta generation in the model of the
6 isolated CA1 network. While it may be expected that isolated theta generation would require local
7 pyramidal cells to provide rhythmic, recurrent excitation to interneurons, our simulations additionally
8 showed that the relatively rare pyramidal cell to pyramidal cell local excitatory connections were also
9 required.

10 Based on our results, we hypothesize that the inhibitory and excitatory connections within CA1
11 that were identified to be critical in our perturbation (“muting”) simulations (Figure 6B) interact
12 to generate the theta waves in the model as follows. Pyramidal cells preferentially discharge at
13 the trough of the LFP analog, strongly recruiting especially the PV+ basket and bistratified cells
14 (green and brown raster plots in Figure 3C), which, in turn, cause a silencing of the pyramidal cells
15 (blue raster plot in Figure 3C) for about the first third of the rising half (i.e., from 0° to about
16 60°) of the LFP analog theta cycle. As the pyramidal cells begin to emerge from this period of strong
17 inhibition, initially only a few, then progressively more and more pyramidal cells reach firing threshold,
18 culminating in the highest firing probability at the theta trough, completing the cycle. The progressive
19 recruitment of pyramidal cells during the theta cycle appears to be paced according to gamma (see blue
20 raster plot in Figure 3C), and it is likely that the intra-CA1 collaterals of the discharging pyramidal
21 cells play key roles in the step-wise (gamma-paced) recruitment of more and more pyramidal cells
22 as the cycle approaches the following trough. The predicted key roles for physiological pyramidal
23 cell to pyramidal cell connections in theta-gamma generation during running may be tested in future
24 experiments.

Rationale for bases of comparison between modeling results with experimental data

Because our model represented the isolated CA1 network, the modeling results were compared with experimental data from the isolated CA1 preparation when possible. Modeling results for which no corresponding experimental data were available from the isolated CA1 preparation, such as the phase preferential firing of individual interneuron types during theta oscillations, were compared with *in vivo* data from anesthetized animals (Figure 5B). Experimental results from anesthetized animals offered the most complete data set (e.g., no experimental data were available on CCK basket cells and neurogliaform cells from awake animals, see Figure 5 - figure supplement 2). Out of the four interneuronal types for which *in vivo* data were available from both the awake and anesthetized conditions (Figure 5 - figure supplement 2), the phase preference of the axo-axonic cell in the model (163°) was closer to the anesthetized phase (185°) than to the awake phase (251°), whereas the PV+ basket cells in the model displayed phase preferential firing (357°) closer to data reported from awake (289° - 310°) than anesthetized animals (234° - 271°); the precise reasons underlying these differences are not yet clear. In contrast, bistratified and O-LM cells fired close to the trough in the model, under anesthesia and in awake animals, potentially indicating the primary importance of pyramidal cell inputs in driving these interneurons to fire during theta oscillations under all conditions.

While our model is fundamentally a model of the rat CA1 (e.g., in terms of cell numbers and connectivity; see Table 3 in Bezaire and Soltesz (2013)), some of the electrophysiology data used for constructing the single cell models (Supplementary Material) came from the mouse. In addition, the experimental data on the isolated CA1 preparation were obtained from both rat (Goutagny et al., 2009) and mouse (Amilhon et al., 2015), similar to the experimental results on the phase specific firing *in vivo* (e.g., awake rat: Lapray et al. (2012); awake mouse: Varga et al. (2014)). Because there is no reported evidence for major, systematic differences in key parameters such as the phase specific firing of rat and mouse interneurons *in vivo*, we did not compare our modeling results with rat and mouse data separately.

1 A final point concerns the nature of the theta rhythm that emerged in our model. In general, the
2 *in vivo* theta rhythm has been reported to be either atropine resistant or atropine sensitive, where the
3 former is typically associated with walking and may not be dependent on neuromodulatory inputs,
4 while the latter requires intact, rhythmic cholinergic inputs (Kramis et al., 1975). Given that our
5 model did not explicitly represent neuromodulatory inputs, it is likely that the theta that emerged
6 from our model most closely resembled the atropine resistant form. However, it is also plausible that
7 both forms of theta benefit from occurring in a network that is predisposed to oscillate at the theta
8 frequency, as the model network results suggested.

9 **An accessible approach to modeling that balances detail, scale, flex-** 10 **ibility and performance**

11 Our results from the strictly data-driven, full-scale CA1 model are consistent with those of earlier
12 models that elegantly demonstrated the basic ingredients capable of producing emergent network os-
13 cillations at a range of frequencies in microcircuits and small networks (Rotstein et al., 2005; Siekmeier,
14 2009; Neymotin et al., 2011b,a; Ferguson et al., 2013). In addition, our modeling approach also pro-
15 vides a full-scale option to advance the recent studies of network activity propagation and information
16 processing during theta (Cutsuridis et al., 2010; Cutsuridis and Hasselmo, 2012; Taxidis et al., 2013;
17 Saudargiene et al., 2015). Here, we demonstrated that emergent theta and gamma oscillations and
18 theta phase preferential firing are possible even as additional interneuron types are incorporated and
19 the network is scaled up to full size with realistic connectivity including 5 billion synapses between
20 the 300,000-plus cells of our network model.

21 This work is one step in our broader effort to build a 1:1 model of the entire temporal lobe us-
22 ing a hypothesis-driven model development process, where at each stage of model development the
23 models are used to address specific questions. For example, here we employed our newly developed
24 full-scale CA1 model to gain mechanistic insights into the ability of the intra-CA1 circuitry to generate
25 theta oscillations (Goutagny et al., 2009). The current CA1 network model can be developed into a
26 whole hippocampal or temporal lobe model by replacing the designed CA3 and entorhinal cortical

1 afferents with biophysically detailed CA3, ECIII, and septal networks. While we design our model
2 networks with the motivation to answer a particular question, we keep in mind their potential usage
3 for a broad range of questions. Previously, we built a dentate gyrus model to study epileptic network
4 dynamics ([Santhakumar et al., 2005](#); [Morgan and Soltesz, 2008](#)) that was then used by several groups
5 to study disparate topics including epilepsy, network mechanisms of inhibition and excitability, sim-
6 ulation optimization, and modeling software ([Migliore et al., 2006](#); [Gleeson et al., 2007](#); [Hines et al.,](#)
7 [2008a,b](#); [Hines and Carnevale, 2008](#); [Thomas et al., 2009](#); [Winkels et al., 2009](#); [Cutsuridis et al., 2010](#);
8 [Jedlicka et al., 2010a,b](#); [Thomas et al., 2010](#); [Tejada and Roque, 2014](#)). Our previous model has
9 demonstrated how the resource intensive process of designing a detailed, large-scale model is offset
10 by its potential usage in numerous ways by a multitude of groups. On the other hand, future efforts
11 will be needed to continue to incorporate experimental data obtained by the scientific community on
12 additional, not yet represented parameters into the platform offered by our full-scale CA1 network
13 model, e.g., on cell type-specific gap junctions and short-term plasticity, neuromodulators, diversity
14 of pyramidal cells, glial dynamics, cell to cell variability (e.g., [Schneider et al. \(2014\)](#)) and others.

15 We developed a flexible and biologically relevant model that uses computational resources effi-
16 ciently, positioning the model to be used by the broader community for many future questions. Im-
17 portantly, the model can be run on the Neuroscience Gateway, an online portal for accessing supercom-
18 puters that does not require technical knowledge of supercomputing (<https://www.nsgportal.org/>).
19 The model is public, well documented, and also well characterized in experimentally relevant terms
20 (See Supplementary Material and online links given in Methods). In addition, all the model configu-
21 rations and simulation result data sets used in this work are available online ([Bezaire et al., 2015](#)) at
22 (<http://doi.org/10.6080/K05H7D60>) so the same simulations can easily be repeated with a future,
23 updated model using SimTracker ([Bezaire et al., 2016](#)). Mindful that this model could be used by
24 people with a broad range of modeling experience, we have made freely available our custom software
25 SimTracker (<http://dx.doi.org/10.1101/081927>) that works with the model code to support each
26 step of the modeling process ([Bezaire et al., 2016](#)).

Conclusion and Outlook

As highlighted by the BRAIN Initiative, there is an increasing recognition in neurobiology that we must compile our collective experimental observations of the brain into something more cohesive and synergistic than what is being conveyed in individual research articles if we are to fully benefit from the knowledge that we collectively produce (Ramaswamy et al., 2015; Markram et al., 2015). By assimilating our collective knowledge into something as functional as a model, we can further probe the gaps in our experimental studies, setting goals for future experimental work. On the other hand, as powerful new tools are gathering vast quantities of neuroscience data, the extraction and organization of the data itself are becoming a challenge. At least three large programs are undertaking this challenge: the Hippocampome project (for neuroanatomical and electrophysiological data in the hippocampus of mice; Wheeler et al. (2015)), the Human Brain Project (currently for neuroanatomical and electrophysiological data and models of the rat neocortex, Ramaswamy et al. (2015)), and NeuroElectro (for electrophysiological data from all species and brain areas; Tripathy et al. (2014)). These comprehensive databases create the opportunity to build strongly biology-inspired models of entire networks, with all the cells and synapses explicitly represented. Such models are not subject to the connectivity scaling tradeoff wherein smaller networks have unrealistically low levels of input or unrealistically high connectivity between cells. In addition, such models are usable for investigations into an almost infinite number of questions at any level from ion channels, to synapses, to cell types, to microcircuit contributions. This approach represents a new strategy in computational neuroscience, distinct from and complementary to the use of more focused models whose role is to highlight the potential mechanism of a small number of network components.

The scale, flexibility, and accessibility of our strictly data-driven, full-scale CA1 model should aid the modeling of other large scale, detailed, biologically constrained neural networks. The current CA1 network model produces results in agreement with experimental data, but also extends the results to probe the mechanisms of spontaneous theta generation. It provides specific testable predictions that enable focused design of future experiments, as well as providing an accessible resource for the broader

1 community to explore mechanisms of spontaneous theta and gamma generation. Because the model
2 is available at full scale, it is a relevant resource for exploring the transformation of incoming spatial
3 and contextual information to outgoing mnemonic engrams as part of spatial and memory processing,
4 and other pertinent network dynamics.

5 **Methods**

6 All results presented in this work were obtained from simulations of computational models. We imple-
7 mented our CA1 model in parallel NEURON 7.4, a neural network simulator ([Carnevale and Hines,](#)
8 [2005](#)). The model simulations were run with a fixed time step between 0.01 and 0.025 ms, for a sim-
9 ulation duration of 2,000 or 4,000 ms (except for Figure 6D where one simulation ran for 1,600 ms).
10 We executed the simulations on several supercomputers, including Blue Waters at the National Cen-
11 ter for Supercomputing Applications at University of Illinois, Stampede and Ranger (retired) at the
12 Texas Advanced Computing Center (TACC), Comet and Trestles at the San Diego Supercomputing
13 Center (SDSC), and the High Performance Computing Cluster at the University of California, Irvine.
14 We used our MATLAB-based SimTracker software tool to design, execute, organize, and analyze the
15 simulations ([Bezaire et al., 2016](#)).

16 **Model Development**

17 The CA1 network model included one type of multicompartmental pyramidal cell with realistic mor-
18 phology and eight types of interneurons with simplified morphology, including PV+ basket cells,
19 CCK+ basket cells, bistratified cells, axo-axonic cells, O-LM cells, Schaffer Collateral-associated cells,
20 neurogliaform cells, and ivy cells.

21 Model neurons sometimes behave much differently than expected when subjected to current sweep
22 protocols or synaptic inputs that are outside the range of the original protocols used to construct
23 the model. To ensure the model cells exhibited robust biophysical behavior in a wide range of net-
24 work conditions, we implemented a standard, thorough characterization strategy for each cell type

1 (Supplementary Material).

2 The behavior of each cell type was characterized using a current injection sweep that matched
3 experimental conditions reported in the literature. Published experimental data was compared side-
4 by-side with model cell simulation results (Supplementary Material). Model cells were connected via
5 NEURON's double exponential synapse mechanism (Exp2Syn), with each connection comprising an
6 experimentally observed number of synapses (see Table 1).

7 The connections between cells were determined with the following algorithm, for each postsynaptic
8 and presynaptic cell type combination:

- 9 1. Calculate the distances between every presynaptic cell and postsynaptic cell of the respective
10 types;
- 11 2. Compute the desired number and distance of connections, as defined by the presynaptic axonal
12 distance distribution and total number of desired connections of this type; the total number of
13 incoming connections expected by each postsynaptic cell type is divided into radial distance bins
14 and distributed among the bins according to the Gaussian axonal bouton distribution of the
15 presynaptic cell;
- 16 3. Assign each of the possible connections determined in step 2 (connections within the axonal
17 extent of the presynaptic cell) to their respective distance bins, and randomly select a specific
18 number of connections from each bin (the specific number calculated to follow the axonal bouton
19 distribution).

20 When determining which cells of the model to connect, we distributed all cells evenly within their
21 respective layers in 3D space and enabled random connectivity for cell connections where the postsy-
22 naptic cell body fell within the axonal extent of the presynaptic cell (looking in the XY plane only).
23 Each time a connection was established between two cells, the presynaptic cell innervated the experi-
24 mentally observed number of synapses on the postsynaptic cell. The synapse locations were randomly
25 chosen from all possible places on the cell where the presynaptic cell type had been experimentally
26 observed to innervate. The random number generator used was NEURON's `nrnRan4int`.

1 Biological Constraints

2 The cell number and connectivity parameters were exactly as we reported previously in our in-depth
3 quantitative assessment of anatomical data about the CA1 ([Bezaire and Soltesz, 2013](#)). In the latter
4 paper that formed the data-base for the current full-scale model, we combined immunohistochemical
5 data about laminar distribution and coexpression of markers to estimate the number of each interneu-
6 ron type in CA1. We then extracted from the experimental literature bouton and input synapse
7 counts for each cell type and multiplied these counts by our estimated number of each cell and de-
8 termined the available input synapses and boutons in each layer of CA1. The number of connections
9 each cell type was likely to make with every other cell type was based on the results of our quan-
10 titative assessment. As the quantitative assessment did not make detailed, interneuron type-specific
11 estimates of connections between interneurons, we performed additional calculations to arrive at the
12 numbers of connections between each type of interneuron in our model. Briefly, we determined the
13 number of inhibitory boutons available for synapsing on interneurons within each layer of CA1. Then,
14 we distributed these connections uniformly across the available incoming inhibitory synapses onto
15 interneurons that we had calculated for that layer. We calculated available incoming synapses by
16 using published experimental observations of inhibitory synapse density on interneuron dendrites by
17 cell class and layer in CA1, which we combined with known anatomical data regarding the dendritic
18 lengths of each interneuron type per layer. We therefore made the following assumption: All available
19 incoming inhibitory synapses onto interneurons in a layer have an equal chance of being innervated by
20 the available inhibitory boutons targeting interneurons in that layer. For further details of the exact
21 calculations, please see the Supplementary Material.

22 The electrophysiology of each cell was tuned using a combination of manual and optimization
23 techniques. We first fit each cell's resting membrane potential, capacitance, time constant, and input
24 resistance, followed by hyperpolarized properties such as the sag amplitude and time constant, followed
25 by subthreshold depolarized properties such as a transient peak response, and finally active properties
26 such as spike threshold, rheobase, firing rate, action potential width, height, and afterhyperpolariza-

1 tion. For some cells, we employed the Multiple Run Fitter tool within NEURON to simultaneously fit
2 multiple ion channel conductances. The characterization of each cell type, as well as its comparison
3 to experimental data from the same cell type, is included in the the Supplementary Material.

4 After fitting the cell model properties, we simulated paired recordings to characterize the connec-
5 tions between our model cells. Where experimental data existed for paired recordings, we matched
6 the experimental holding potential and synapse reversal potential, then performed 10 different paired
7 recordings. We characterized the average synapse properties from those 10 runs, including the synap-
8 tic amplitude, 10% - 90% rise time, and decay time constant. Finally, we tuned the synaptic weights
9 and time constants to fit our averages to the experimental data.

10 To determine the synaptic weights and kinetics for those connections that have not yet been
11 experimentally characterized, we used a novel modeling strategy we call Network Clamp, described in
12 [Bezaire et al. \(2016\)](#). As experimental paired recording data were not available to directly constrain
13 the synapse properties, we instead constrained the firing rate of the cell in the context of the *in*
14 *vivo* network, for which experimental data have been published. We innervated the cell with the
15 connections it was expected to receive *in vivo*, and then sent artificial spike trains through those
16 connections, ensuring that the properties of the spike trains matched the behavior expected from each
17 cell *in vivo* during theta (firing rate, level of theta modulation, preferred theta firing phase). Next,
18 we adjusted the weight of the afferent excitatory synapses onto the cell (starting from experimentally
19 observed values for other connections involving that cell type) until the cell achieved a realistic firing
20 rate similar to had been experimentally observed *in vivo*.

21 Stimulation

22 As none of the model neurons in the CA1 network are spontaneously active, it was necessary to pro-
23 vide excitatory input to them by stimulating their CA3 and entorhinal cortex synapses. Although the
24 model code is structured to allow the addition of detailed CA3 and cortical inputs, the stimulation
25 patterns used in the present study were not representative of the information content thought to be
26 carried via inputs from those areas, because the focus was on the function of the CA1 network in iso-

1 lation from rhythmic extra-CA1 influences. In accordance with experimental evidence of spontaneous
2 neurotransmitter release ([Kavalali, 2015](#)), we modeled the activation of CA3 and entorhinal synapses
3 as independent Poisson stochastic processes. The model neurons were connected to a subset of these
4 afferents, such that they received a constant level of excitatory synaptic input.

5 We constrained the synapse numbers and positions of the stimulating afferents using anatomical
6 data. To constrain the afferent synapse weights, we used an iterative process to determine the com-
7 binations of synaptic weights that enabled most of the interneurons to fire similar to their observed
8 *in vivo* firing rates ([Figure 5 - figure supplement 1](#) and [Table 6](#)). First, we used the output of an
9 initial full-scale simulation to run network clamp simulations on a single interneuron type, altering
10 the incoming afferent synapse weights (but not the incoming spike trains) until the interneuron type
11 fired at a reasonable rate. Then, we applied the synaptic weight to the afferent connections onto that
12 interneuron type in the full-scale model. The resulting simulation then led to a new network dynamic
13 as the constrained activity of that interneuron type caused changes in other interneuron activity. We
14 then performed this exercise for each interneuron type as necessary until we achieved a network where
15 all cell types participated without firing at too high of a level. CCK+ cells had a steep response to
16 the weight of the incoming afferent synapses, remaining silent until the weight was increased signifi-
17 cantly and then spiking at a high rate, see [Figure 5 - figure supplement 1](#); the particular difficulty in
18 obtaining the *in vivo* observed firing rate for CCK+ cells in the model may indicate that *in vivo* they
19 may be strongly regulated by extra-CA1 inhibitory inputs (e.g., from the lateral entorhinal cortex;
20 see [Basu et al. \(2016\)](#) that are not included in the isolated CA1 model).

21 **Analysis of Simulation Results**

22 We analyzed the results of each simulation with standard neural data analysis methods provided
23 by our SimTracker software ([Bezaire et al., 2016](#)), including the spike density function (SDF) of all
24 pyramidal neuron spikes ([Szűcs, 1998](#)), the periodogram of the SDF, and the spectrogram of the LFP
25 analog. We determined the dominant theta and gamma frequencies for the network as the peak in
26 the power spectral density estimate obtained by the spectrogram, and confirmed that those peaks

1 are identical for the SDF and the LFP analog. After finding a dominant theta or gamma frequency,
2 we then analyzed the level of modulation and preferred firing phase for each cell type. Finally, we
3 calculated the firing rate of each cell type.

4 **LFP analog**

5 We calculated an approximation of the LFP generated by the model neurons based on the method
6 described by [Schomburg et al. \(2012\)](#). For each pyramidal cell within 100 μm of a reference electrode
7 location in stratum pyramidale (coordinates = longitudinal: 200 μm ; transverse: 500 μm ; height
8 from base of stratum oriens: 120 μm), the contribution to extracellular potential at each point along
9 the dendritic and axonal morphology was recorded using NEURON's extracellular mechanism and
10 scaled in inverse proportion to the distance from the electrode. In order to reduce the computational
11 load of the simulation, 10% of the pyramidal cells outside the 100 μm radius were randomly selected;
12 their distance-scaled extracellular potentials were scaled up by a factor of 10 and then added to the
13 contributions of the inner cells. We performed reference simulations and LFP analog calculations with
14 the inner radius set to 200 μm and 500 μm and obtained results identical with those in [Figures 3 and](#)
15 [4](#) (where an inner radius of 100 μm was used), except for negligible increases in the theta oscillation
16 power found in the LFP analog spectrogram.

17 **Spike Density Function**

18 We calculated the spike density function (SDF) of all pyramidal cell spikes using a Gaussian kernel
19 with a window of 3 ms and a bin size of 1 ms ([Szűcs, 1998](#)). To see how a cell's spiking activity is
20 related to its SDF, see [Figure 4 - figure supplement 1](#).

21 **Oscillations**

22 To quantify the frequency and power of the oscillations of the network, we computed a one-sided
23 Welch's Periodogram of the SDF ([Colgin et al., 2009](#)) using a Hamming window with 50% over-

1 lap. To characterize the stability of the theta oscillation, we ran the control network for 4 sec-
2 onds and then computed the spectrogram of the SDF and of the LFP analog using an analysis
3 script from [Goutagny et al. \(2009\)](#) based on the `mtspecgramc` function from the Chronux toolbox
4 (<http://chronux.org/>).

5 Spike Phases and Theta Modulation

6 We calculated the preferred firing theta phases of each cell, using all the spikes of that cell type that
7 occurred after the first 50 ms of the simulation, relative to the filtered LFP analog. The spike times
8 were converted to theta phases, relative to the troughs of the LFP analog theta cycle in which they
9 fired. We then subjected the spike phases to a Rayleigh test to determine the level of theta modulation
10 of the firing of each cell type ([Varga et al., 2014](#)).

11 Firing Rates

12 The firing rates of the cells were calculated by cropping the first 50 ms of the simulation to remove the
13 initial effects, and then dividing the resulting number of spikes of each cell type by the total number of
14 cells of that type and the duration of the simulation. An alternate average firing rate was calculated by
15 dividing by the number of active cells of that type rather than all of the cells of that type, which gave
16 the average firing rate over all firing cells instead, to better compare with experimentally observed
17 firing rate averages.

18 Statistical Comparison of Theta Power

19 For the GABA_B-related simulations, we ran three of each condition and then performed an ANOVA
20 to test for significance in the difference of theta power among the conditions.

Cross correlation of theta and gamma

To investigate whether a relationship existed between the simultaneous theta and gamma oscillations found in the LFP analog of our control simulation, we filtered the LFP analog signal within the theta range (5-10 Hz) and the gamma range (25-80 Hz). We applied a Hilbert transform to each filtered signal and then compared the phase of the theta-filtered signal with the envelope of the gamma-filtered signal to determine the extent to which theta could modulate the gamma oscillation.

Accessibility

Our model code is available online at ModelDB (code version used to produce results in this work: <https://senselab.med.yale.edu/ModelDB/showModel.cshtml?model=187604>) and Open Source Brain (most recent code version: http://opensourcebrain.org/projects/nc_ca1). Open Source Brain provides tools for users to characterize and inspect model components. The model is also characterized online at <http://mariannebezaire.com/models/ca1>, along with a graphical explanation of our quantitative assessment used to constrain the model connectivity [Bezaire and Soltesz \(2013\)](#), as well as links to our model code and model results, and detailed instruction manuals for our NEURON code and SimTracker tool ([Bezaire et al., 2016](#)).

For those who wish to view and analyze our simulation results without rerunning the simulation, our simulation results are available on CRCNS.org at <http://doi.org/10.6080/K05H7D60> and can be freely accessed after obtaining a free account ([Bezaire et al., 2015](#)). Our analyses of these data can be recreated using our publically available SimTracker tool.

Our custom software tool, SimTracker is further discussed in our companion paper, [Bezaire et al. \(2016\)](#). SimTracker is freely available online at <http://mariannebezaire.com/simtracker/> and is also listed in SimToolDB at <https://senselab.med.yale.edu/SimToolDB/showTool.cshtml?Tool=153281>. The tool is offered both as a stand-alone, compiled version for those without access to MATLAB (for Windows, Mac OS X, and Linux operating systems), and as a collection of MATLAB scripts for those with

1 MATLAB access.

2 Acknowledgements

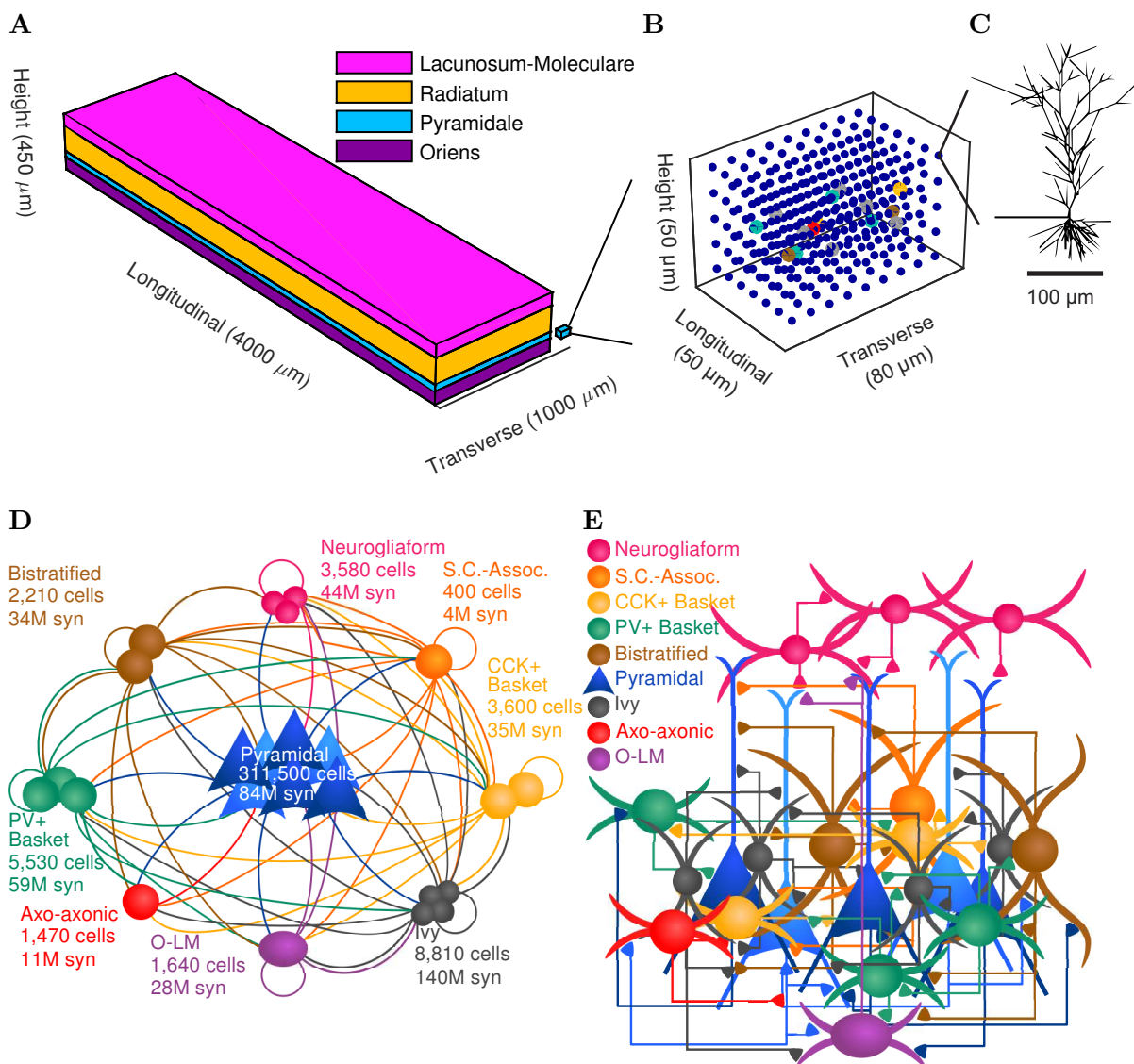
3 Immeasurable support was provided by NEURON developers Michael Hines and Ted Carnevale un-
4 der NIH NINDS grant R01-NS11613 (to M.H.) and NSF grant 1458495 (to T.C.). This work used
5 the Extreme Science and Engineering Discovery Environment (XSEDE), which is supported by Na-
6 tional Science Foundation grant number ACI-1053575; the project was supported by XSEDE Re-
7 search Allocation grant TG-IBN140007 (to I.S., M.B. and I.R.) and XSEDE Startup Allocations to
8 I.S. (TG-IBN130022) and M.B. (TG-IBN100011) and via the Neuroscience Gateway with the sup-
9 port of NSF grants 1458840 and 1146949 (to Majumdar et al.). The authors acknowledge the Texas
10 Advanced Computing Center (TACC) at The University of Texas at Austin for providing high perfor-
11 mance computing resources that have contributed to the research results reported within this paper
12 (<http://www.tacc.utexas.edu>). Additionally, this research is part of the Blue Waters sustained-
13 petascale computing project, which is supported by the National Science Foundation (awards OCI-
14 0725070 and ACI-1238993) and the state of Illinois. Blue Waters is a joint effort of the University
15 of Illinois at Urbana-Champaign and its National Center for Supercomputing Applications (NCSA).
16 Parallel supercomputers used in this work include: Blue Waters, owned by the University of Illinois
17 and NCSA; Stampede and the retired Ranger, owned by the University of Texas' Texas Advanced
18 Computing Center (TACC); Trestles and Comet, owned by the San Diego Supercomputing Center;
19 University of California at Irvine's High Performance Computer and the retired Broadcom Distributed
20 Unified Cluster.

21 We would like to thank the University of Texas' Texas Advanced Computing Center team, the San
22 Diego Supercomputing Center and Neuroscience Gateway teams (especially Glenn Lockwood, Amitava
23 Majumdar, Subhashini Sivagnanam, Mahidhar Tatineni, and Kenneth Yoshimoto), and UC Irvine's
24 HPC team (especially Joseph Farran and Harry Mangalam) for their excellent technical support
25 throughout this work. We would also like to thank Padraig Gleeson, Andras Ecker, Tom Morse, and

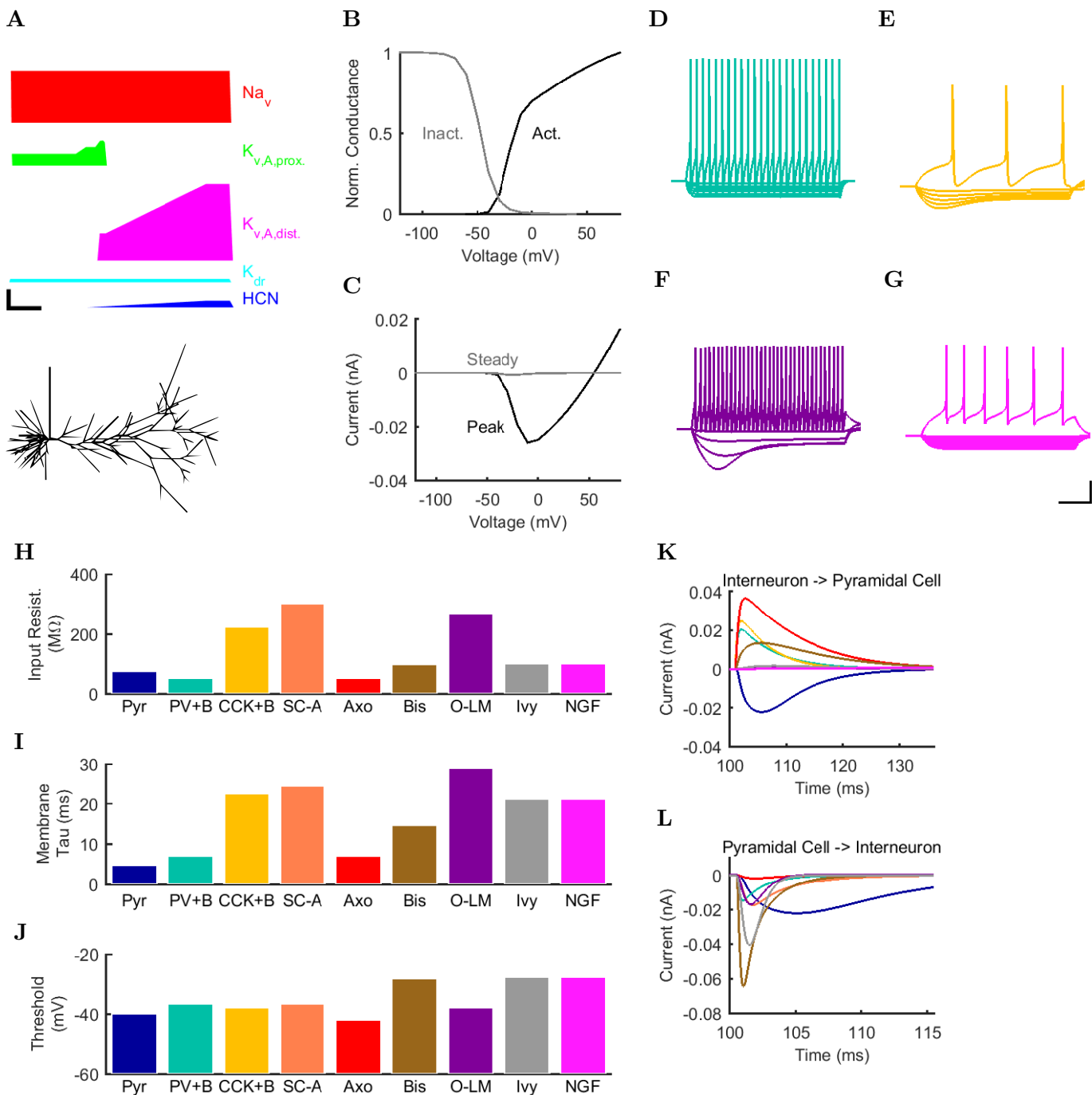
- 1 Jeff Teeters for assistance making our code and model results public, and Jesse Jackson and Sylvain
- 2 Williams for the use of their spectrogram analysis script.

1

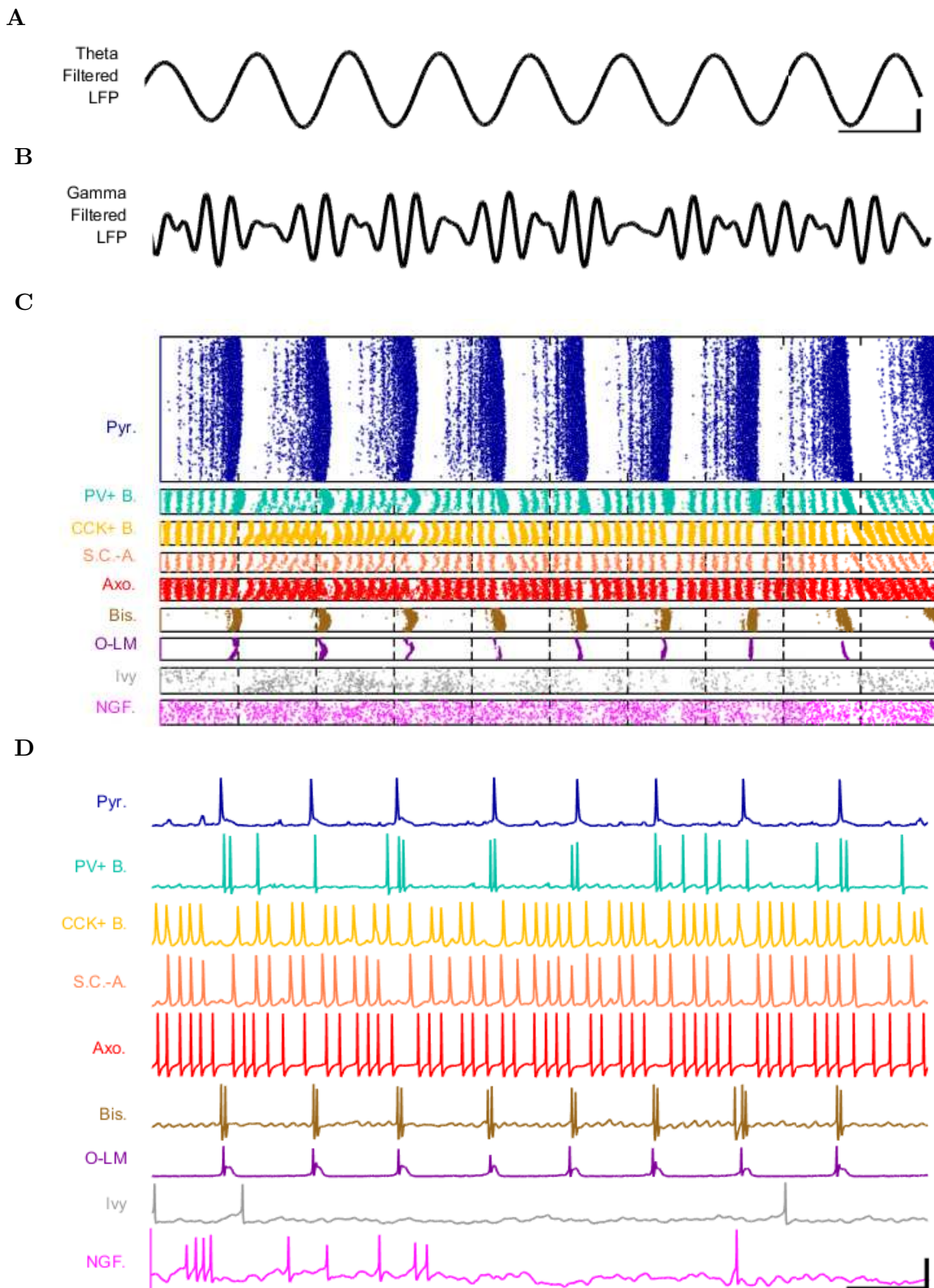
Figures



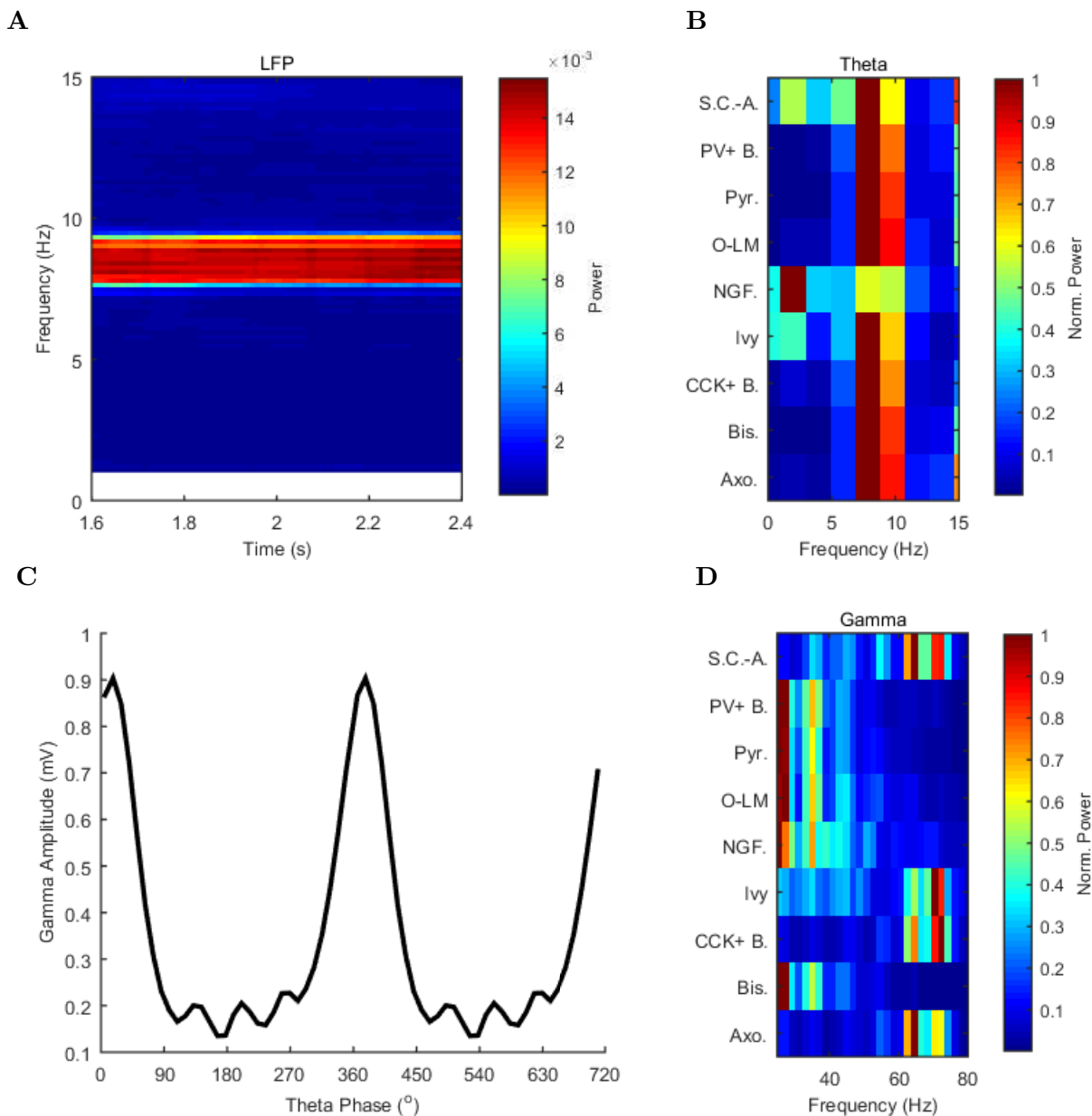
1 **Figure 1: CA1 network connectivity.** (A) The model network is arranged in a layered
 2 prism with the lengths of each dimension similar to the actual dimensions of the CA1 region
 3 and its layers. (B) The model cell somata within a small chunk of stratum pyramidale (as
 4 depicted in A) are plotted to show the regular distribution of model cells throughout the layer
 5 in which they are found. (C) Each pyramidal cell in the network has detailed morphology
 6 with realistic incoming synapse placement along the dendrites and soma. (D-E) Diagrams
 7 illustrate connectivity between types of cells. (D) The network includes one principal cell type
 8 (pyramidal cells) and eight interneuron types. Cell types that may connect are linked by a
 9 line colored according to the presynaptic cell type. Most cell types can connect to most other
 10 cell types. Total number of cells of each type are displayed, as are the number of local output
 11 synapses (boutons) from all cells of each type. (E) The number, position, and cell types of
 12 each connection are biologically constrained, as are the numbers and positions of the cells. See
 13 Figure 1 - figure supplement 1 for details about the convergence onto each cell type. Also see
 14 Table 1 and Figure 1 - figure supplement 2 for information about the cell-type combinations
 15 of the 5 billion connections and the axonal distributions followed by each cell type, as well as
 16 detailed connectivity results at <http://doi.org/10.6080/K05H7D60>.



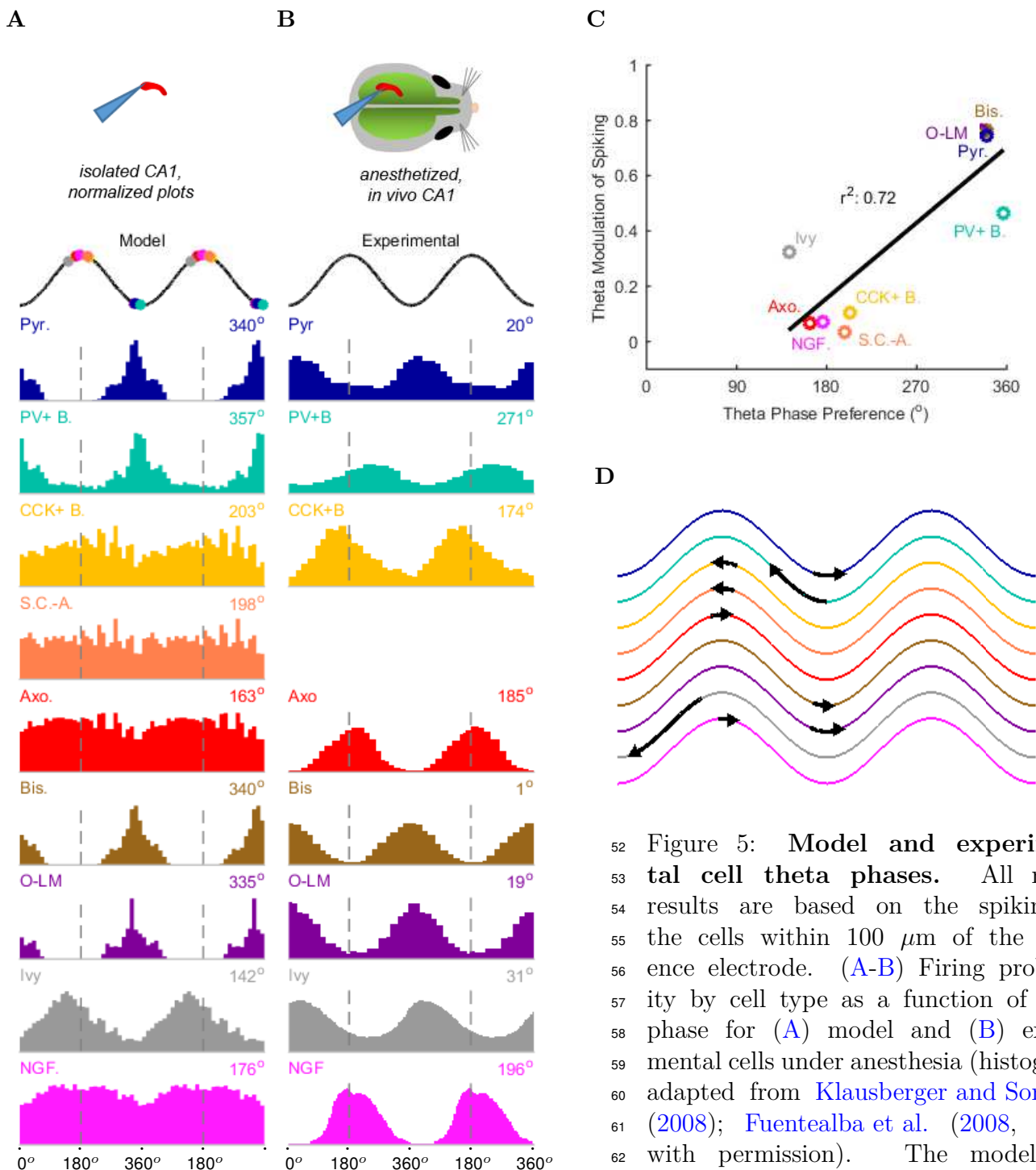
17 **Figure 2: Electrophysiology of the model network components.** (A) Ion channel densities vary as a function of location (top) in the morphologically detailed pyramidal cell model
 18 (bottom; adapted from Poolos et al. (2002)). Scale bar: 100 μm and 0.01 $\mu\text{F}/\text{cm}^2$. (B - C)
 19 The sodium channel found in the pyramidal cell soma is characterized in terms of (B) the activa-
 20 tion/inactivation curves and (C) the current-voltage relation at peak (transient) current and
 21 steady state. (D - (G)) Current sweeps are shown for 4 model cell types: (D) PV+ basket cell,
 22 (E) CCK+ basket cell, (F) O-LM cell, and (G) neurogliaform cell. Scale bar: 100 ms and 20
 23 mV. (H-J) Electrophysiological properties for each cell type, including (H) input resistance, (I)
 24 membrane time constant, and (J) action potential threshold. (K - L) Pyramidal cell synap-
 25 tic connections are characterized as post-synaptic currents with the postsynaptic cell voltage
 26 clamped at -50 mV; (K) synapses made onto the pyramidal cell from all other cell types and
 27 (L) synapses made by the pyramidal cell onto all network cell types. Cells represented by same
 28 colors as in Figure 1. Source Data available at Figure 2 - Source Data.zip. Additional details
 29 available in the Methods, Table 3, and the Supplementary Material.
 30



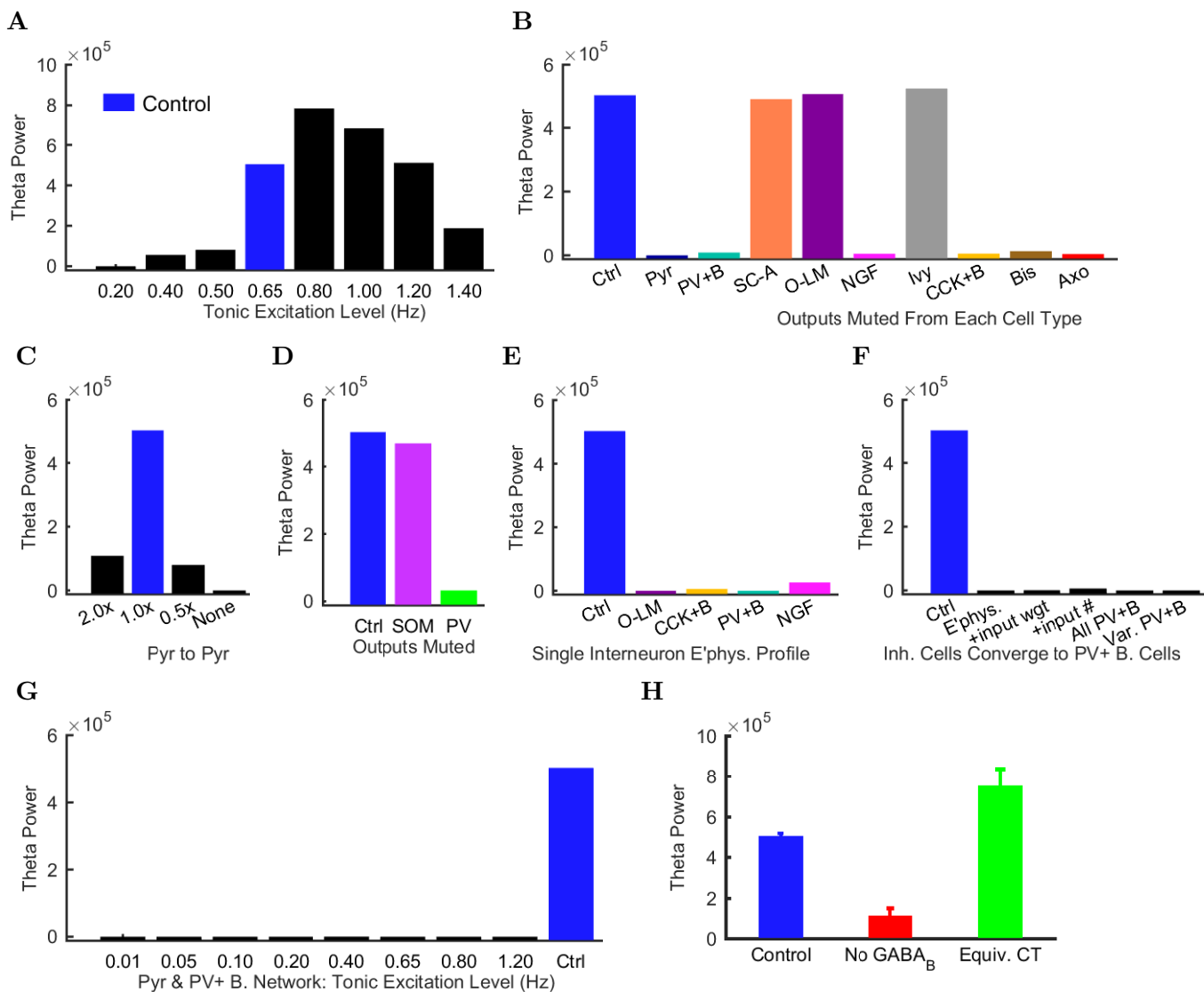
31 **Figure 3: Detailed network activity.** (A-D) One second of network activity is shown. (A -
32 B) The LFP analog, filtered at (A) the theta range of 5-10 Hz and (B) the low gamma range of
33 25-40 Hz, shows consistent theta and gamma signals. Scale bar represents 100 ms and 0.2 mV
34 (theta) or 0.27 mV (gamma) for filtered LFP traces. (C) Raster of all spikes from cells within
35 100 μm of the reference electrode point. (D) Representative intracellular somatic membrane
36 potential traces from cells near the reference electrode point. Scale bar represents 100 ms and
37 50 mV for the intracellular traces. Source Data available at Figure 3 - Source Data.zip.



38 **Figure 4: Spectral analysis of model activity.** (A) A spectrogram of the local pyramidal-
 39 layer LFP analog (including contributions from all pyramidal cells within $100 \mu\text{m}$ of the reference
 40 electrode and 10% of pyramidal cells outside that radius) shows the stability and strength of
 41 the theta oscillation over time. The oscillation also featured strong harmonics at multiples of
 42 the theta frequency of 7.8 Hz. (B,D) Welch's periodogram of the spike density function for
 43 each cell type, normalized by cell type and by displayed frequency range, shows the dominant
 44 network frequencies of (B) theta (7.8 Hz) and (D) gamma (71 Hz). Power is normalized to the
 45 peak power displayed in the power spectrum for each cell type. (C) Cross-frequency coupling
 46 between theta and gamma components of the LFP analog shows that the gamma oscillation is
 47 theta modulated. The gamma envelope is a function of the theta phase with the largest ampli-
 48 tude gamma oscillations occurring at the trough of the theta oscillation. Following convention,
 49 the theta trough was designated $0^\circ/360^\circ$; see e.g., Varga et al. (2012). A graphical explana-
 50 tion of the relation between a spike train and its spike density function is shown in Figure
 51 4 - figure supplement 1. Source Data available for this figure at Figure 4 - Source Data.zip.



52 **Figure 5: Model and experimental cell theta phases.** All model
 53 results are based on the spiking of the cells within 100 μm of the refer-
 54 ence electrode. (A-B) Firing probability by cell type as a function of theta
 55 phase for (A) model and (B) exper-
 56 mental cells under anesthesia (histograms
 57 adapted from Klausberger and Somogyi
 58 (2008); Fuentealba et al. (2008, 2010)
 59 with permission). The model his-
 60 tograms are normalized; see Figure
 61 5 - figure supplement 1 for firing rates.
 62 (C) Theta phase preference and theta
 63 modulation level were correlated; better
 64 modulated cell types spiked closer to the
 65 LFP analog trough near the phase prefer-
 66 ence of pyramidal cells. (D) Theta
 67 phase preference plotted on an idealized
 68 LFP wave for model data (base of ar-
 69 row signifies model phase preference and
 70 head of arrow shows distance to anes-
 71 thetized, experimental phase preference).
 72 Source Data available at Figure 5 - Source
 73 Data.zip.
 74
 75
 76



77 **Figure 6: Altered network configurations.** Oscillation power (in mV^2/Hz) of the spike density
 78 function (SDF) for pyramidal cells within $100 \mu\text{m}$ of the reference electrode, at the peak
 79 frequency within theta range (5-10 Hz) in altered network configurations. For corresponding
 80 peak frequencies, see Figure 6 - figure supplement 1. (A) Theta is present at some excitation
 81 levels. (B) Muting each cell type's output caused a range of effects. (C) The stability and
 82 frequency of spontaneous theta in the network was sensitive to the presence and number of
 83 recurrent connections between CA1 pyramidal cells. (D) Partially muting the broad classes
 84 of PV+ or SOM+ cells by 50% showed that PV+ muting disrupted the network more than
 85 SOM+ muting. (E) Theta falls apart when all interneurons are given the same electrophysi-
 86 ological profile, whether it be of a PV+ basket, CCK+ basket, neurogliaform, or O-LM cell.
 87 (F) Gradually setting all interneuron properties to those of PV+ basket cells did not restore
 88 theta. From left to right: control network; PV+ basket cell electrophysiology; also weights of
 89 incoming synapses; also numbers of incoming synapses; then all interneurons being PV+ basket
 90 cells (with the addition of the output synapse numbers, weights, and kinetics); then variable
 91 RMP (normal distribution with standard deviation of 8 mV). (G) A wide range in excitation
 92 was unable to produce theta in the PV+ B. network. (H) Removing the GABA_B component
 93 from the neurogliaform synapses onto other neurogliaform cells and pyramidal cells showed a
 94 significant drop in theta power. Massively increasing the weight of the GABA_A component
 95 to produce a similar amount of charge transfer restored theta power (compare the IPSCs cor-
 96 responding to each condition in Figure 6 - figure supplement 2). Standard deviations ($n=3$)
 97 shown; significance ($p=1.8\text{e-}05$). Source Data available at Figure 6 - Source Data.zip.

Tables

Pre/Post	Axo	Bis	CCK+B	Ivy	NGF	O-LM	Pyr	PV+B	SC-A
Axo	0.00e+00	0.00e+00	0.00e+00	0.00e+00	0.00e+00	0.00e+00	1.12e+07	0.00e+00	0.00e+00
Bis	2.35e+05	3.54e+05	5.76e+05	2.64e+05	0.00e+00	6.40e+05	3.12e+07	8.85e+05	6.80e+04
CCK+B	1.41e+05	2.12e+05	9.79e+05	5.64e+05	0.00e+00	2.62e+05	3.24e+07	5.31e+05	8.32e+04
Ivy	3.53e+05	5.30e+05	3.42e+06	2.11e+06	1.00e+06	2.23e+06	1.28e+08	1.33e+06	4.08e+05
NGF	0.00e+00	0.00e+00	0.00e+00	0.00e+00	6.09e+05	0.00e+00	4.36e+07	0.00e+00	0.00e+00
O-LM	1.18e+05	1.77e+05	1.44e+06	0.00e+00	4.65e+05	9.84e+04	2.49e+07	4.42e+05	1.60e+05
Pyr	7.19e+05	2.43e+06	0.00e+00	2.38e+05	0.00e+00	1.17e+07	6.14e+07	7.03e+06	1.26e+05
PV+B	5.73e+04	8.62e+04	1.37e+05	7.05e+04	0.00e+00	0.00e+00	5.83e+07	2.16e+05	9.60e+03
SC-A	8.82e+03	1.33e+04	1.30e+05	1.06e+05	0.00e+00	1.97e+04	3.74e+06	3.32e+04	1.44e+04
CA3	1.23e+07	2.56e+07	1.44e+07	3.39e+07	0.00e+00	0.00e+00	3.73e+09	6.69e+07	1.55e+06
ECIII	1.43e+06	1.91e+06	4.02e+06	0.00e+00	3.75e+06	0.00e+00	8.09e+08	0.00e+00	4.58e+05

98 Table 1: Number of synapses between each cell type. Connections between cells generally comprise 1 - 10 synapses each. Presynaptic
 99 cells are listed down the first column (corresponding to each row) and postsynaptic cells are listed along the first row (corresponding
 100 to each column).

Supercomputer	# Processors	Sim Time (s)	Exchange Time (s)	Load Balance
Comet	1680	2610.28	1.05	0.999
Comet	1704	2566.76	0.65	0.999
Comet	1728	2601.22	0.86	0.999
Comet via NSG	1728	2060.88	0.83	0.999
Stampede via NSG	2048	2471.64	1.71	1.000
Stampede	2048	2578.32	0.29	1.000
Stampede	2528	2189.56	1.78	0.999
Stampede	3008	1844.22	0.91	0.999
Stampede	3488	1641.91	0.86	0.999

¹⁰¹ Table 2: Simulation time, exchange time, and load balance for simulations executed on various
¹⁰² supercomputers and numbers of processors.

Condition	Pyr	PV+B	CCK+B	SC-A	Axo	Bis	O-LM	Ivy	NGF
Resting Membrane Potential (mV)	-63.0	-65.0	-70.6	-70.5	-65.0	-67.0	-71.5	-60.0	-60.0
Input Resistance ($M\Omega$)	62.2	52.0	211.0	272.4	52.0	98.7	343.8	100.0	100.0
Membrane Tau (ms)	4.8	6.9	22.6	24.4	7.0	14.7	22.4	21.1	21.1
Rheobase (pA)	250.0	300.0	60.0	40.0	200.0	350.0	50.0	160.0	170.0
Threshold (mV)	52.0	-36.6	-40.6	-43.1	-41.6	-28.1	100.2	-27.6	-27.7
Delay to 1st Spike (ms)	12.4	74.6	166.6	127.7	43.5	28.4	8.9	173.3	119.0
Half-Width (ms)	80.7	0.9	1.9	1.6	0.6	0.5	112.9	0.6	0.6

103 Table 3: Electrophysiological characteristics of each model cell type. For more information about model electrophysiology, see the
 104 Supplementary Material.

Cell Type	Hyper. (pA)	Step Size (pA)	Depol. (pA)
PV+ B.	-300	50	+500
CCK+ B.	-100	20	+80
O-LM	-130	30	+80
NGF	-130	20	+190

105 Table 4: Current injection levels used to characterize interneuron current sweeps in Figure
 106 [2D-2G](#).

Cell Type	Firing Rate (Hz)	Modulation Level	p	Phase (0° =trough)
Axo.	8.9	0.07	4.58e-130	163.4
Bis.	18.0	0.76	0.00e+00	340.0
CCK+ B.	54.4	0.10	0.00e+00	202.8
Ivy	43.3	0.33	0.00e+00	142.1
NGF.	55.1	0.07	1.46e-32	176.3
O-LM	17.4	0.76	0.00e+00	334.7
Pyr.	6.0	0.74	0.00e+00	339.7
PV+ B.	0.9	0.46	0.00e+00	356.8
S.C.-A.	5.2	0.03	1.13e-07	197.9

107 Table 5: Preferred theta firing phases for each model cell type.

Cell Type	Firing Rate (Hz)			Theta Phase ($^{\circ}$)	State of Animal	Animal	Ref.
	Theta	Non	SWR				
ADI	8.60	0.06	0.25	156	anesth: u+k & x	rat	Klausberger et al. (2005)
Axo-axonic	17.10	3.50	2.95	185	anesth: u+k & x	rat	Klausberger et al. (2003)
Axo-axonic	27		27	251	awake, head restraint	mouse	Varga et al. (2014)
Bistratified	5.90	0.90	42.80	1	anesth: u+k & x	rat	Klausberger et al. (2004)
Bistratified	34		36	0	awake, head restraint	mouse	Varga et al. (2014)
Bistratified	30.42	27.65	35.82	2	awake	rat	Katona et al. (2014)
CCK+ Basket	9.40	1.60	2.70	174	anesth: u+k & x	rat	Klausberger et al. (2005)
Ivy	0.70	1.70	0.80	31	anesth: u+k & x	rat	Fuentealba et al. (2008)
Ivy	2.80	2.10	5.20	46	awake, free	rat	Lapray et al. (2012)
Ivy	2.40	3.00	6.70		awake, free	rat	Fuentealba et al. (2008)
NGF	6.00	2.65	2.30	196	anesth: u+k & x	rat	Fuentealba et al. (2010)
O-LM	4.90	2.30	0.23	19	anesth: u+k & x	rat	Klausberger et al. (2003)
O-LM	29.80	10.40	25.40	346	awake, head restraint	mouse	Varga et al. (2012)
O-LM	17.30	11.88	18.95	342	awake	rat	Katona et al. (2014)
PPA	5.75	1.95	1.50	100	anesth: u+k & x	rat	Klausberger et al. (2005)
PV+ Basket	7.30	2.74	32.68	271	anesth: u+k & x	rat	Klausberger et al. (2003)
PV+ Basket				234	anesth: u+k & x	rat	Klausberger et al. (2005)
PV+ Basket	21.00	6.50	122.00	289	awake, free	rat	Lapray et al. (2012)
PV+ Basket	25.00	8.20	75.00	307	awake, head restraint	mouse	Varga et al. (2012)
PV+ Basket	28		77	310	awake, head restraint	mouse	Varga et al. (2014)
Pyramidal				20	anesth: u+k & x	rat	Klausberger et al. (2003)
Trilaminar	0.20	0.10	69.00	trough	anesth: u+k & x	rat	Ferraguti et al. (2005)
Double Proj.	0.90	0.55	26.93	77	anesth: u+k & x	rat	Jinno et al. (2007)
Oriens Retro.	0.53	0.37	53.37	28	anesth: u+k & x	rat	Jinno et al. (2007)
Radiatum Retro.	5.15	1.90	0.70	298	anesth: u+k & x	rat	Jinno et al. (2007)

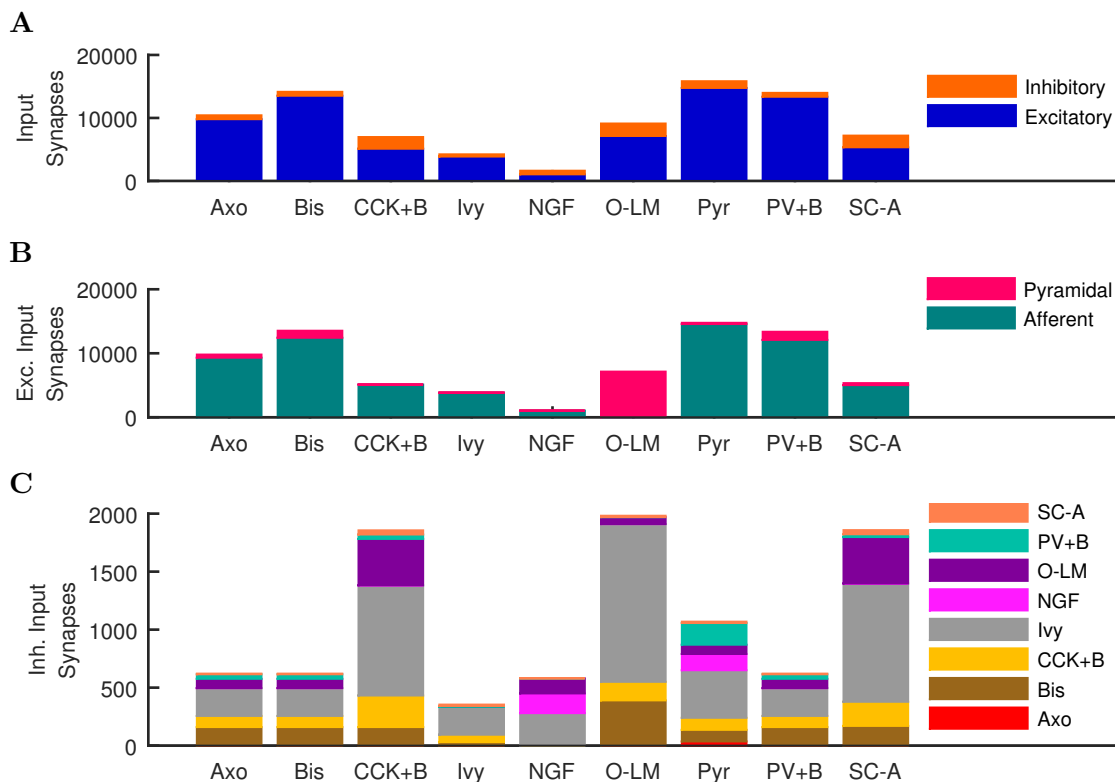
108 Table 6: Firing rates and theta phase preferences for various cell types in various conditions. Theta phase is relative to the LFP
 109 recorded in the pyramidal layer, where 0° and 360° are at the trough of the oscillation. non: non-theta/non-SWR state. SWR:
 110 sharp wave/ripple. u+k & x: urethane + supplemental doses of ketamine and xylazine.

Condition	Theta		Gamma		Overall	
	Frequency	Power	Frequency	Power	Frequency	Power
Tonic Excitation Level (Hz)						
0.20	n/a	0.0e+00	n/a	0.0e+00	n/a	0.0e+00
0.40	5.9	5.6e+04	25.4	4.1e+04	13.7	6.5e+04
0.50	9.8	8.1e+04	25.4	1.0e+05	19.5	5.6e+05
0.65 (Ctrl.)	7.8	5.0e+05	25.4	2.0e+05	7.8	5.0e+05
0.80	9.8	7.8e+05	29.3	2.6e+05	9.8	7.8e+05
1.00	9.8	6.8e+05	29.3	1.4e+05	9.8	6.8e+05
1.20	9.8	5.1e+05	33.2	1.8e+05	11.7	8.2e+05
1.40	9.8	1.9e+05	25.4	3.4e+05	11.7	8.6e+05
Single Interneuron E'phys. Profile						
Ctrl	7.8	5.0e+05	25.4	2.0e+05	7.8	5.0e+05
O-LM	n/a	0.0e+00	n/a	0.0e+00	n/a	0.0e+00
CCK+B	9.8	5.7e+03	62.5	6.9e+05	62.5	6.9e+05
PV+B	n/a	0.0e+00	n/a	0.0e+00	n/a	0.0e+00
NGF	5.9	2.6e+04	39.1	2.4e+06	39.1	2.4e+06
Inh. Cells Converge to PV+ B. Cells						
Ctrl	7.8	5.0e+05	25.4	2.0e+05	7.8	5.0e+05
E'phys.	n/a	0.0e+00	n/a	0.0e+00	n/a	0.0e+00
+input wgt	7.8	6.8e+02	44.9	1.6e+06	21.5	3.4e+06
+input #	9.8	6.1e+03	31.3	1.1e+06	15.6	2.0e+06
All PV+B	n/a	0.0e+00	n/a	0.0e+00	n/a	0.0e+00
Var. PV+B	n/a	0.0e+00	n/a	0.0e+00	n/a	0.0e+00
Outputs Muted						
Ctrl	7.8	5.0e+05	25.4	2.0e+05	7.8	5.0e+05
SOM	7.8	4.7e+05	27.3	1.4e+05	7.8	4.7e+05
PV	9.8	3.2e+04	27.3	8.1e+05	13.7	1.5e+06
Pyr to Pyr						
2.0x	9.8	1.1e+05	25.4	7.3e+05	13.7	1.0e+06
1.0x (Ctrl.)	7.8	5.0e+05	25.4	2.0e+05	7.8	5.0e+05
0.5x	7.8	8.0e+04	29.3	2.2e+05	29.3	2.2e+05
None	9.8	1.1e+00	70.3	3.7e+01	70.3	3.7e+01
Outputs Muted From Each Cell Type						
Ctrl	7.8	5.0e+05	25.4	2.0e+05	7.8	5.0e+05
Pyr	7.8	1.1e+00	70.3	3.8e+01	70.3	3.8e+01
PV+B	9.8	8.8e+03	29.3	1.9e+06	29.3	1.9e+06
SC-A	9.8	4.9e+05	27.3	1.8e+05	9.8	4.9e+05
O-LM	7.8	5.1e+05	25.4	8.3e+04	7.8	5.1e+05
NGF	9.8	5.2e+03	27.3	9.1e+05	13.7	1.6e+06
Ivy	7.8	5.3e+05	25.4	2.0e+05	7.8	5.3e+05
CCK+B	5.9	5.5e+03	25.4	3.3e+03	3.9	5.7e+03
Bis	5.9	1.3e+04	29.3	1.7e+06	29.3	1.7e+06
Axo	7.8	4.0e+03	33.2	1.2e+06	15.6	1.9e+06
Pyr & PV+ B. Network: Tonic Excitation Level (Hz)						
0.01	n/a	0.0e+00	n/a	0.0e+00	n/a	0.0e+00
0.05	n/a	0.0e+00	n/a	0.0e+00	n/a	0.0e+00
0.10	n/a	0.0e+00	n/a	0.0e+00	n/a	0.0e+00
0.20	n/a	0.0e+00	n/a	0.0e+00	n/a	0.0e+00
0.40	5.9	2.3e+02	25.4	1.2e+02	3.9	2.4e+02
0.65	n/a	0.0e+00	n/a	0.0e+00	n/a	0.0e+00
0.80	n/a	0.0e+00	n/a	0.0e+00	n/a	0.0e+00
1.20	n/a	0.0e+00	n/a	0.0e+00	n/a	0.0e+00
Ctrl	7.8	5.0e+05	25.4	2.0e+05	7.8	5.0e+05

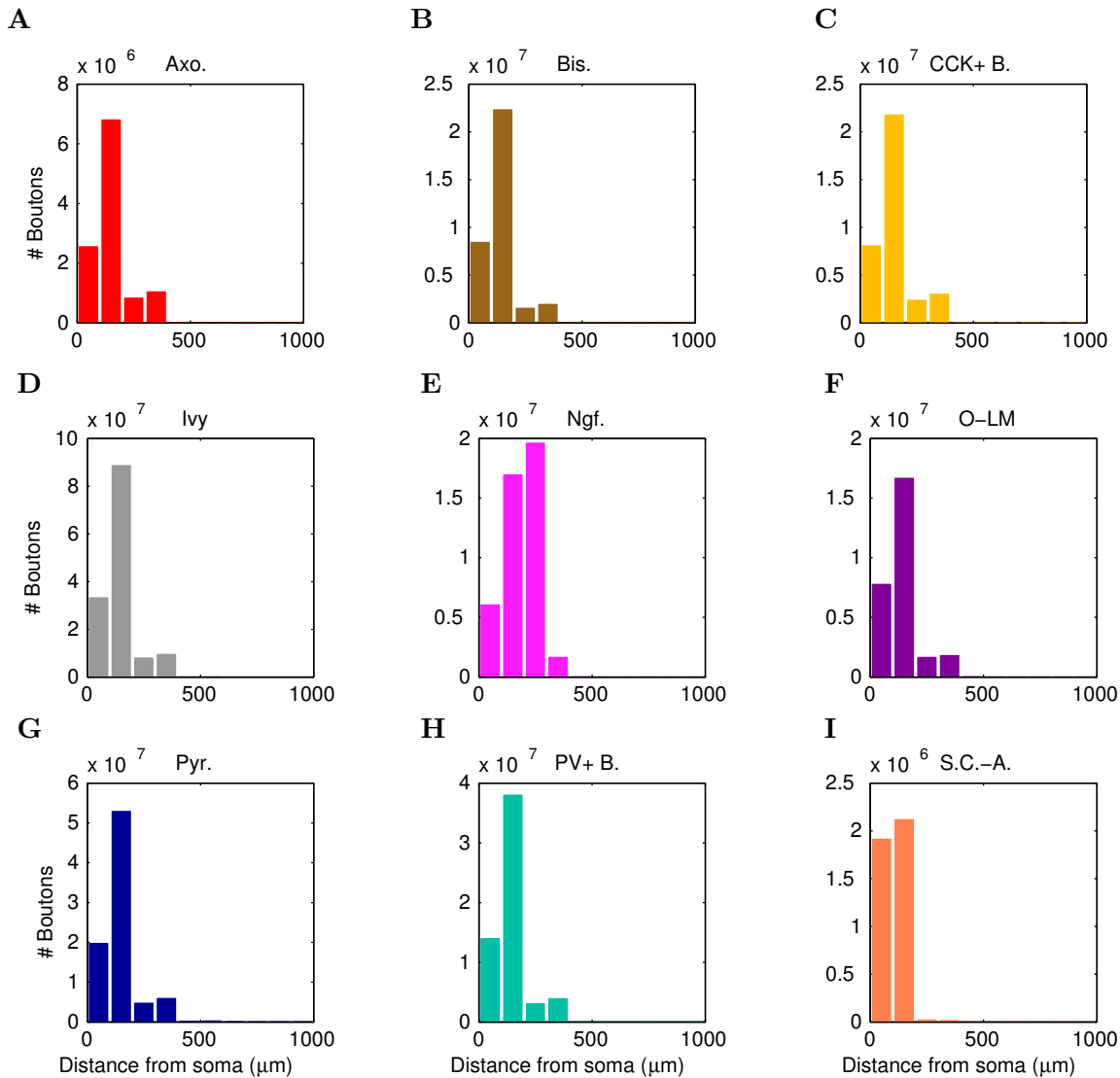
111 Table 7: Peak, theta and gamma frequencies and powers of the pyramidal cell spike density
 112 function using Welch's Periodogram. As in Figure 6 - figure supplement 1, networks where no
 113 pyramidal cells spiked - resulting in zero power within the spectral analysis of the pyramidal
 114 cell spike density function - have their peak frequencies listed as "n/a" for "not available".

1

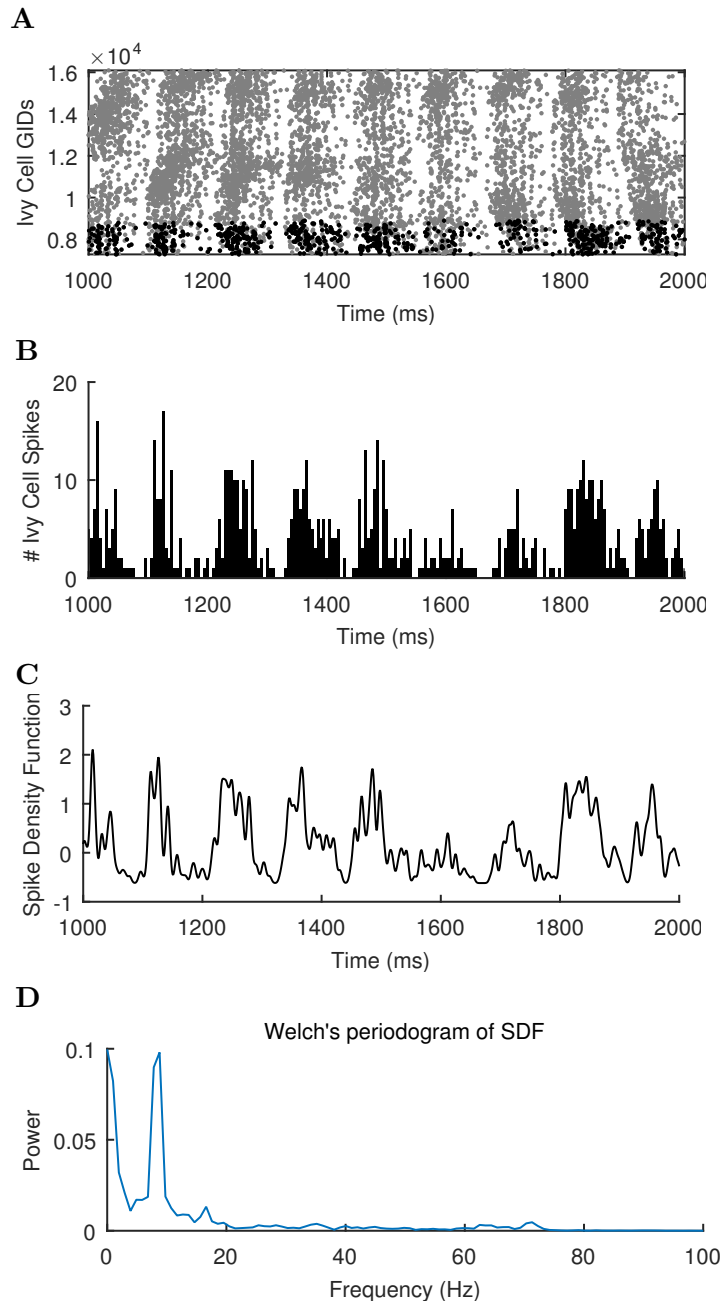
Figure Supplements



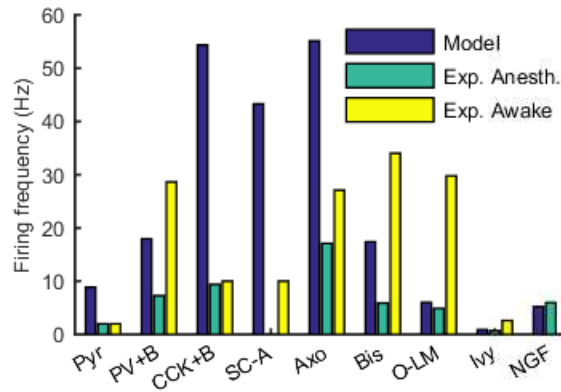
115 Figure 1 - figure supplement 1: **Quantitative Network Connectivity**. The average number
 116 of incoming synapses per postsynaptic cell of the given type are shown for (A) all inputs to the
 117 cells, (B) all excitatory inputs to the cells and (C) all inhibitory inputs to the cells.



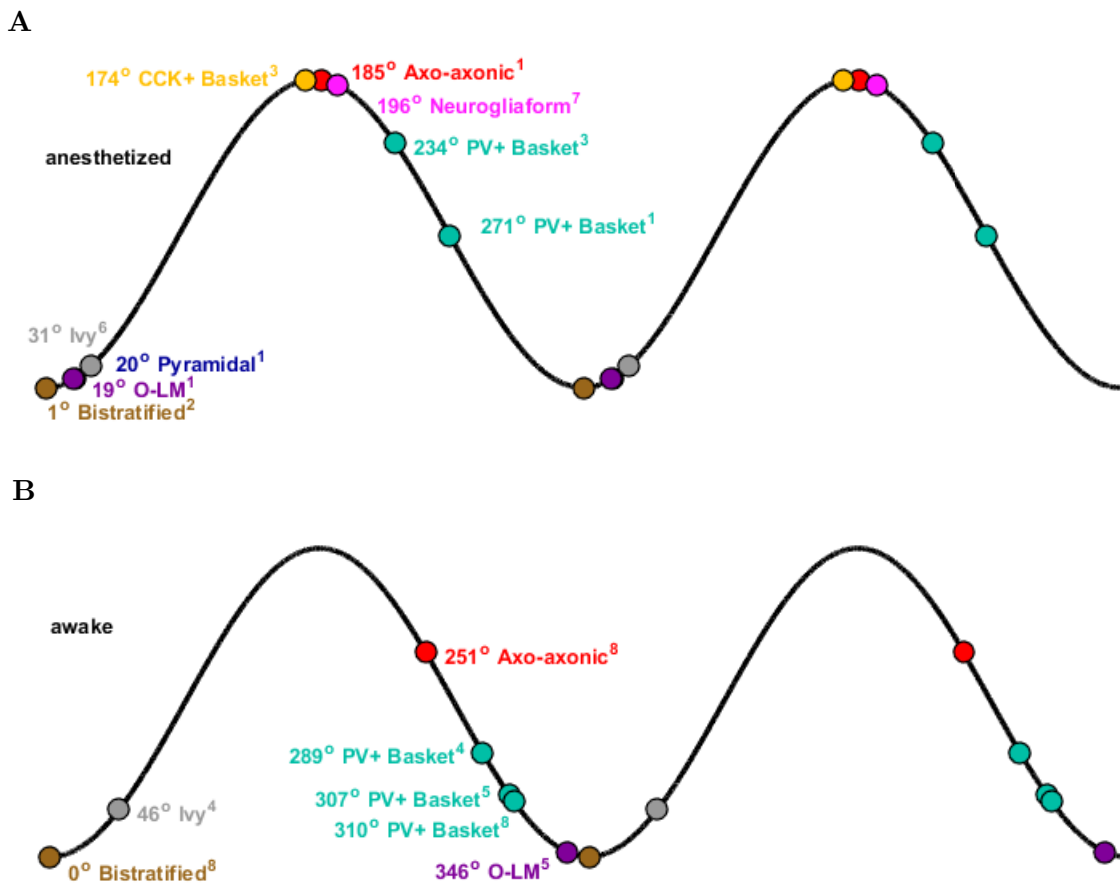
118 Figure 1 - figure supplement 2: **Anatomically constrained connectivity.** The axonal dis-
 119 tributions are shown per presynaptic cell type. The distribution of boutons is plotted as a
 120 function of distance from the presynaptic cell's soma. Boutons connecting to all possible types
 121 of postsynaptic cells are included in the plot. The colors correspond to each presynaptic cell
 122 type using the same color code as previous figures.



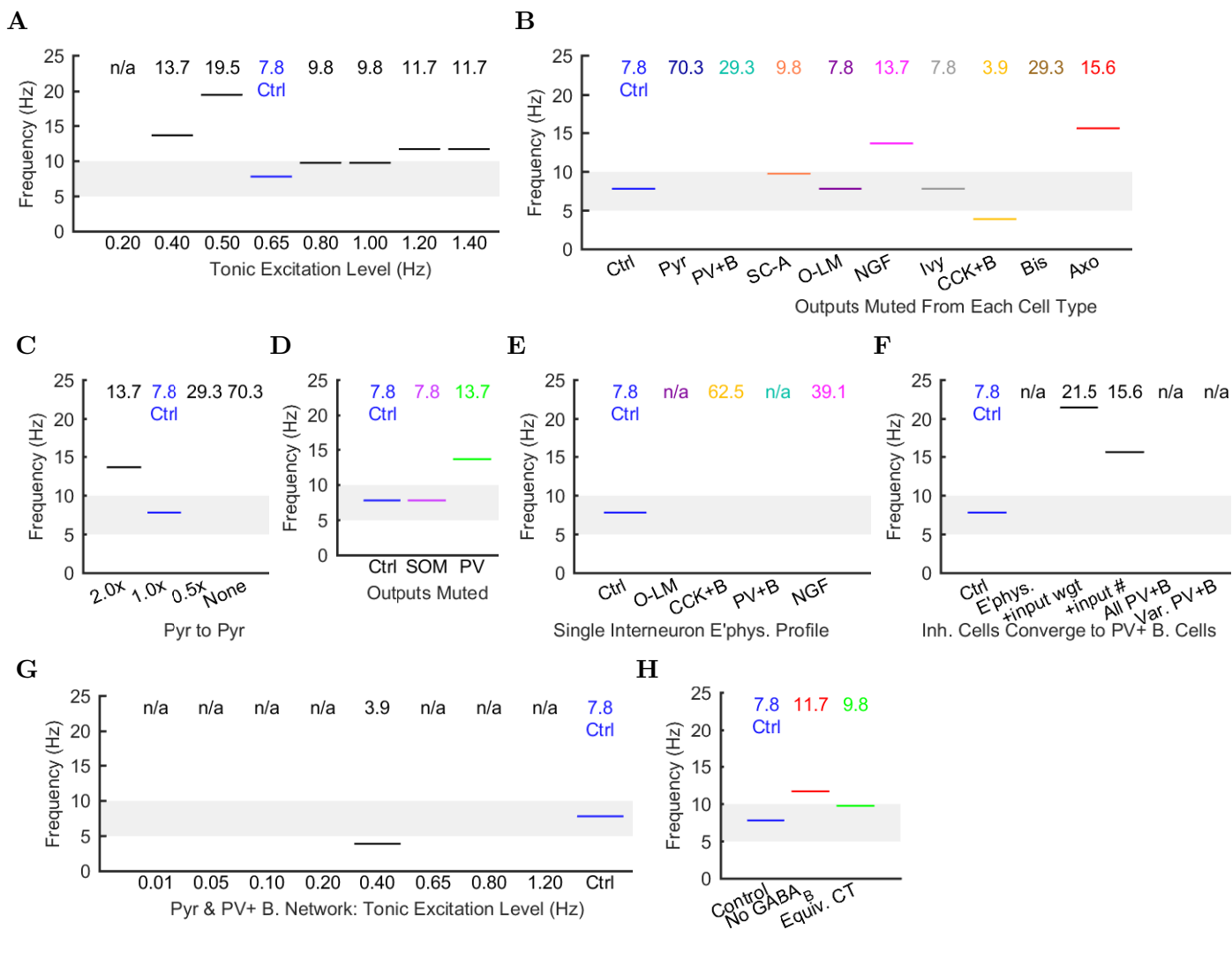
123 Figure 4 - figure supplement 1: **Different views of cell activity.** Several ways of characteriz-
124 ing model cell activity per cell type are shown using the spikes from the ivy cells as an example.
125 (A) The spike times of each ivy cell are plotted as a function of time and ivy cell number. A
126 subset of ivy cells positioned within $100 \mu\text{m}$ of the reference electrode location (whose spikes are
127 shown in black) are then carried forward in the remaining calculations. (B) The spikes of the
128 local ivy cells are binned into 1 ms windows to give spike counts per window. (C) A continuous
129 representation of the ivy cell spikes as a function of time is given in the spike density function
130 (SDF) computed from the ivy cell spike times. (D) A Welch's Periodogram is computed, which
131 summarizes the power of each oscillation frequency in the ivy cell SDF. Although only a part
132 of the simulation is shown, the full simulation length (except the first 50 ms) was used in the
133 spectral analysis.



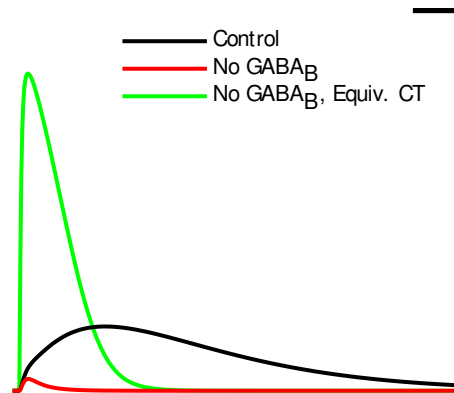
134 Figure 5 - figure supplement 1: **Firing rates of model and experimental cells of each**
 135 **type**. For experimental cells, firing rates in both the anesthetized and awake states were
 136 included where available. See Table 6 for sources of experimental data.



137 Figure 5 - figure supplement 2: **Theta phase-specific firing preferences of various biolog-**
 138 **ical hippocampal cell types as reported in the literature**. The trough of the pyramidal-
 139 layer LFP is designated as 0°/360° and the peak as 180°. There is variation in phase preference
 140 for given cell types as a function of experimental preparation. Shown are (A) anesthetized and
 141 (B) awake experimental conditions. Reference subscripts correspond to: 1: Klausberger et al.
 142 (2003), 2: Klausberger et al. (2004), 3: Klausberger et al. (2005), 4: Lapray et al. (2012), 5:
 143 Varga et al. (2012), 6: Fuentealba et al. (2008), 7: Fuentealba et al. (2010), 8: Varga et al.
 144 (2014). See Table 6 for further details.



145 **Figure 6 - figure supplement 1: Peak Frequencies of Oscillations in Altered Networks.**
 146 Peak theta frequency (within 5-10 Hz) of the spike density function (SDF) for all pyramidal cells
 147 within 100 μm of the reference electrode in each altered network configuration. For networks
 148 where no pyramidal cells spiked, resulting in zero power within the spectral analysis of the
 149 pyramidal cell spike density function, their peak frequencies are listed as “not available” or
 150 “n/a”. (A) Spontaneous theta oscillation accelerated out of theta range with more excitation.
 151 (B) Muting each cell type shifted the oscillation out of range (neurogliaform, CCK+ basket,
 152 and axo-axonic cells), disrupted theta but not gamma (not shown; pyramidal, PV+ basket,
 153 and bistratified cells), or had little effect (S.C.-A., O-LM, and ivy cells). (C) Doubling the
 154 connections between CA1 pyramidal cells increased the theta frequency, while networks with
 155 half the number or no recurrent collaterals lost the slow oscillation but kept gamma. (D)
 156 Removing 50% of PV+ cell inhibition (PV+ basket, bistratified, and axo-axonic cells) or 50%
 157 of SOM+ cell inhibition (bistratified or O-LM cells) shifted the oscillation out of theta range or
 158 lost the slow oscillation entirely but kept gamma. (E) Peak oscillation shifted out of theta range
 159 when all interneurons had the same electrophysiological profile, regardless of the profile used.
 160 (F) Converging all properties to PV+ basket cells, gamma was restored (not shown) but not
 161 theta (left to right: control; network with 1: diverse interneurons with same electrophysiology; 2:
 162 also with same weights of incoming synapses; 3: also with same numbers of incoming synapses;
 163 4: complete conversion to PV+ basket cells; 5: added variability in resting membrane potential
 164 (normal distribution with st. dev. = 8 mV)). (G) In the all-PV+ basket cell network, a
 165 wide range of excitation levels could not produce a spontaneous theta rhythm. (H) Removing
 166 GABA_B increased the oscillation frequency.



167 Figure 6 - figure supplement 2: **IPSCs from the neurogliaform to pyramidal cell synapse**
168 **corresponding to the different conditions in Figure 6H.** These traces are from pyramidal
169 cells clamped at -50 mV during a paired recording from a presynaptic neurogliaform cell with a
170 GABA_A reversal potential of -60 mV and a GABA_B reversal potential of -90 mV. The currents
171 shown are averages from 10 recordings. Scale bar = 100 ms and 5 pA.

Source Data Files

Figure 2 - Source Data

Included are data for voltage and current clamp data for ion channel, single cell, and synaptic characterizations. For the four interneuron types with current injection sweeps displayed, a separate file is provided for each injection in the sweep, with the naming convention trace_[cell type]_[current injection level].dat, where the current injection level is given in pA. For all interneuron types, the current injection sweep data has also been gathered into an AxoClamp ATF (tab-delimited) style of file, to allow for (re)calculation of cell properties according to the processes used for calculations from biological recordings. These files follow the naming convention of [celltype].atf.

The ion channel characterized in this figure was an Na_v channel, inserted into a single compartment cell of diameter and length 16.8 microns (a soma) with a density such that the maximum, macroscopic conductance was $.001 \mu\text{S}/\text{cm}^2$. The reversal potential of the channel was +55 mV and the settings during the characterization protocol were: temperature=34 degrees Celsius, axial resistance = 210 ohm*cm, $[\text{Ca}^{2+}]_{\text{internal}} = 5.0000\text{e-}06$ mM, specific membrane capacitance = $1 \mu\text{F}/\text{cm}^2$. For activation steps, the cell was held at -120 mV and then stepped to potential levels ranging from -60 mV to +80 mV. For inactivation steps, the cell was held at various potential levels ranging from -120 mV to +40 mV for 500 ms and then stepped to +20 mV. Each current injection step is recorded in a separate file, with activation step files following the name convention of `step_to_[stepped-to potential in mV].dat` and inactivation step files following the name convention of `hold_[held-at potential in mV].dat`.

For the synaptic responses, the postsynaptic cell was voltage-clamped at -50 mV and the reversal potential of the synapse was kept at its natural (as defined in the network model code) potential. A spike was triggered in the presynaptic cell and the current response was measured in the postsynaptic cell at the soma. This recording was repeated 10 times, with a randomly chosen connection location each time, and the response was then averaged. In all paired recordings with the pyramidal cell as postsynaptic cell, the sodium channels were blocked to prevent a suprathreshold response. The file convention for paired recordings is `[presynaptic cell].[postsynaptic cell].[Recording #].dat`

- 1 • stepto_[stepped-to potential in mV].dat
- 2 • hold_[held-at potential in mV].dat
- 3 • trace_[cell type]_[current injection level].dat
- 4 • [celltype].atf

5 **Figure 3 - Source Data**

6 This zip file contains 3 files. First, it includes the LFP.dat file which contains the raw, theta-filtered,
7 and gamma-filtered LFP analog traces (the raw local field potential (LFP) analog was calculated
8 from the network activity as detailed in the Methods section). Second, the zip file contains Mem-
9 brane_Potentials.txt, which includes the full duration, intracellular somatic membrane potential
10 recordings from the specific cells shown in Figure 3. Third, it includes the SpikeRasterLocal.dat
11 file which includes the spike times for the length of the entire simulation, from the specific cells dis-
12 played in raster shown in Figure 3. The spike times of every single cell in the network are available
13 in the CRCNS repository. Note that the displayed spike raster in Figure 3 has been downsampled in
14 such a way as to preserve its visual appearance while reducing the image size and load time.

- 15 • FilteredLFP.dat
- 16 • Membrane_Potentials.txt
- 17 • SpikeRasterLocal.dat

18 **Figure 4 - Source Data**

19 This zip file contains the All_SDF_Ctrl_Condition.txt file. The file includes the Spike Density
20 Functions (SDFs) of each cell type in the control network. The calculation of the Spike Density
21 Function is detailed in the Methods section. The power spectra of the SDFs shown in Figure 4 were
22 obtained via a one-sided periodogram using Welch's method where segments have a 50% overlap with
23 a Hamming Window. The spectra for each cell type was normalized to itself so that each cell type

1 could use the full range of colors in the colorbar to show the shape of its spectra, despite different
2 absolute peak powers for different cell types. Note that the spectrogram was computed from the raw
3 LFP analog trace (included in the source data of Figure 3) using the method detailed in Goutagny et
4 al (2009). The cross-frequency coupling was illustrated by performing a Hilbert transform on the raw
5 LFP analog trace to extract the theta phase and gamma envelope as a function of time.

- 6 • LFP.dat
- 7 • All_SDF_Ctrl_Condition.txt

8 **Figure 5 - Source Data**

9 This zip file contains a celltype.txt file that summarizes information about each cell type in the
10 model, and it contains one file per each cell type, with the name convention Spike_Phase_Time_[cell
11 type].txt. The Spike_Phase_Time_* files list, for each cell type, the spike times from all of the cells
12 of that type, and calculated theta phases (relative to the theta-filtered LFP analog) of each spike.
13 From the list of spike phases per cell type, the preferred theta phase, level of theta modulation, and
14 statistical significance were calculated for each cell type using a Rayleigh test for circular data (Varga
15 et al, 2014). The average firing rates of each cell type were obtained by dividing the total number of
16 spikes by the length of the simulation (4000 ms) and by the number of cells of each type (listed in the
17 celltype.txt file).

- 18 • Spike_Phase_Time_*cell.txt
- 19 • celltype.txt

20 **Figure 6 - Source Data**

21 This zip file contains two files. First, it includes a tab-delimited text file called Pyramidal_SDF_All_Conditions.txt,
22 which contains the full length Spike Density Function computed at a resolution of 1000 Hz from the
23 spikes of all pyramidal cells within the local range of the electrode point in the model network, for each
24 network condition studied in Figure 6. Second, it contains a file called Mapping_Network_Condition.txt

1 that maps the names of the simulations (used in the header of Pyramidal_SDF_All_Conditions.txt)
2 to the bar labels in the graphs of Figure 6.

3 The spike times of all pyramidal cells from all network conditions (from which the SDFs were
4 computed) are available online within the CRCNS repository at <http://doi.org/10.6080/K05H7D60>
5 and the calculation of the Spike Density Function is detailed in the Methods section. The power
6 spectra of the SDFs included here were obtained via a one-sided periodogram using Welch's method
7 where segments have a 50% overlap and a Hamming Window. The highest power within the theta
8 oscillation frequency range of 5 - 10 Hz is reported in Figure 6, and the frequency at which the highest
9 power occurred is reported in Figure 6 - figure supplement 2. Table 6 also lists the power and frequency
10 for each condition.

11 Figure 6F included three statistically independent simulations from each network condition (control
12 + two experimental conditions). We performed a one-way analysis of variance (ANOVA) of the peak
13 power of the pyramidal cell SDF within the theta frequency range, including all three simulations
14 from each of the three conditions, grouped by condition.

- 15 • Pyramidal_SDF_All_Conditions.txt
- 16 • Mapping_Network_Condition.txt

References

- 1
- 2 Akam T. E. and Kullmann D. M. Efficient “communication through coherence” requires oscillations
3 structured to minimize interference between signals. *PLoS Comput Biol*, 8(11):e1002760, 2012. doi:
4 10.1371/journal.pcbi.1002760.
- 5 Amilhon B., Huh C. Y., Manseau F., Ducharme G., Nichol H., Adamantidis A., and Williams S.
6 Parvalbumin interneurons of hippocampus tune population activity at theta frequency. *Neuron*, 86
7 (5):1277–1289, 2015. doi: 10.1016/j.neuron.2015.05.027.
- 8 Andersen P., Morris R., Amaral D., Bliss T., and O’Keefe J. *The hippocampus book*. Oxford University
9 Press, USA, 2006. doi: 10.1093/acprof:oso/9780195100273.001.0001.
- 10 Armstrong C. and Soltesz I. Basket cell dichotomy in microcircuit function. *The Journal of physiology*,
11 590(4):683–694, 2012. doi: 10.1113/jphysiol.2011.223669.
- 12 Basu J., Zaremba J. D., Cheung S. K., Hitti F. L., Zemelman B. V., Losonczy A., and Siegelbaum S. A.
13 Gating of hippocampal activity, plasticity, and memory by entorhinal cortex long-range inhibition.
14 *Science*, 351(6269):aaa5694, 2016.
- 15 Belluscio M. A., Mizuseki K., Schmidt R., Kempter R., and Buzsáki G. Cross-frequency phase–phase
16 coupling between theta and gamma oscillations in the hippocampus. *The Journal of Neuroscience*,
17 32(2):423–435, 2012. doi: 10.1523/JNEUROSCI.4122-11.2012.
- 18 Bezaire M. J. and Soltesz I. Quantitative assessment of CA1 local circuits: knowledge base for
19 interneuron-pyramidal cell connectivity. *Hippocampus*, 23(9):751–785, 2013. doi: 10.1002/hipo.
20 22141.
- 21 Bezaire M. J., Raikov I., Burk K., Vyas D., and Soltesz I. Simulation results from full scale and
22 rationally reduced network models of the isolated hippocampal CA1 subfield in rat. *CRCNS.org*,
23 2015. doi: 10.6080/K05H7D60.

- 1 Bezaire M. J., Raikov I., Burk K., Armstrong C., and Soltesz I. SimTracker: a tool and code template
2 to design, manage and analyze neural network model simulations in parallel NEURON. *bioRxiv*,
3 2016. doi: 10.1101/081927.
- 4 Bragin A., Jandó G., Nádasdy Z., Hetke J., Wise K., and Buzsáki G. Gamma (40-100 Hz) oscillation
5 in the hippocampus of the behaving rat. *The Journal of Neuroscience*, 15(1):47–60, 1995.
- 6 Butler J. L., Mendonça P. R., Robinson H. P., and Paulsen O. Intrinsic Cornu Ammonis Area 1
7 theta-nested gamma oscillations induced by optogenetic theta frequency stimulation. *The Journal*
8 *of Neuroscience*, 36(15):4155–4169, 2016. doi: 10.1523/JNEUROSCI.3150-15.2016.
- 9 Buzsáki G. Theta oscillations in the hippocampus. *Neuron*, 33(3):325–340, 2002. doi: 10.1016/
10 S0896-6273(02)00586-X.
- 11 Buzsáki G. and Moser E. I. Memory, navigation and theta rhythm in the hippocampal-entorhinal
12 system. *Nature neuroscience*, 16(2):130–138, 2013. doi: 10.1038/nn.3304.
- 13 Buzsáki G., Buhl D., Harris K., Csicsvari J., Czeh B., and Morozov A. Hippocampal network patterns
14 of activity in the mouse. *Neuroscience*, 116(1):201–211, 2003. doi: 10.1016/S0306-4522(02)00669-3.
- 15 Buzsáki G., Anastassiou C. A., and Koch C. The origin of extracellular fields and currents—EEG,
16 ECoG, LFP and spikes. *Nature reviews neuroscience*, 13(6):407–420, 2012. doi: 10.1038/nrn3241.
- 17 Capogna M. Neurogliaform cells and other interneurons of stratum lacunosum-moleculare gate
18 entorhinal–hippocampal dialogue. *The Journal of physiology*, 589(8):1875–1883, 2011. doi:
19 10.1113/jphysiol.2010.201004.
- 20 Carnevale N. T. and Hines M. L. *The NEURON Book*. Cambridge University Press, New York, 2005.
- 21 Colgin L. L. Mechanisms and functions of theta rhythms. *Annual review of neuroscience*, 36:295–312,
22 2013. doi: 10.1146/annurev-neuro-062012-170330.
- 23 Colgin L. L. Rhythms of the hippocampal network. *Nature Reviews Neuroscience*, 2016. doi: 10.
24 1038/nrn.2016.21.

- 1 Colgin L. L. and Moser E. I. Gamma oscillations in the hippocampus. *Physiology*, 25(5):319–329,
2 2010. doi: 10.1152/physiol.00021.2010.
- 3 Colgin L. L., Denninger T., Fyhn M., Hafting T., Bonnevie T., Jensen O., Moser M.-B., and Moser
4 E. I. Frequency of gamma oscillations routes flow of information in the hippocampus. *Nature*, 462
5 (7271):353–357, 2009. doi: 10.1038/nature08573.
- 6 Craig M. T. and McBain C. J. The emerging role of GABA B receptors as regulators of network
7 dynamics: fast actions from a ‘slow’ receptor? *Current opinion in neurobiology*, 26:15–21, 2014. doi:
8 10.1016/j.conb.2013.10.002.
- 9 Csicsvari J., Hirase H., Czurkó A., Mamiya A., and Buzsáki G. Oscillatory coupling of hippocampal
10 pyramidal cells and interneurons in the behaving rat. *The Journal of neuroscience*, 19(1):274–287,
11 1999.
- 12 Cutsuridis V. and Hasselmo M. GABAergic contributions to gating, timing, and phase precession of
13 hippocampal neuronal activity during theta oscillations. *Hippocampus*, 2012. doi: 10.1002/hipo.
14 21002.
- 15 Cutsuridis V., Cobb S., and Graham B. P. Encoding and retrieval in a model of the hippocampal
16 CA1 microcircuit. *Hippocampus*, 20(3):423–446, 2010. doi: 10.1002/hipo.20661.
- 17 Dannenberg H., Pabst M., Braganza O., Schoch S., Niediek J., Bayraktar M., Mormann F., and
18 Beck H. Synergy of direct and indirect cholinergic septo-hippocampal pathways coordinates firing
19 in hippocampal networks. *The Journal of Neuroscience*, 35(22):8394–8410, 2015. doi: 10.1523/
20 JNEUROSCI.4460-14.2015.
- 21 Dyhrfeld-Johnsen J., Santhakumar V., Morgan R. J., Huerta R., Tsimring L., and Soltesz I. Topolog-
22 ical determinants of epileptogenesis in large-scale structural and functional models of the dentate
23 gyrus derived from experimental data. *Journal of neurophysiology*, 97(2):1566–1587, 2007. doi:
24 10.1152/jn.00950.2006.

- 1 Engel A. K. and Fries P. Beta-band oscillations—signalling the status quo? *Current opinion in*
2 *neurobiology*, 20(2):156–165, 2010. doi: 10.1016/j.conb.2010.02.015.
- 3 Ferguson K. A., Huh C. Y., Amilhon B., Williams S., and Skinner F. K. Experimentally constrained
4 CA1 fast-firing parvalbumin-positive interneuron network models exhibit sharp transitions into
5 coherent high frequency rhythms. *Frontiers in computational neuroscience*, 7, 2013. doi: 10.3389/
6 fncom.2013.00144.
- 7 Ferguson K. A., Huh C. Y., Amilhon B., Manseau F., Williams S., and Skinner F. K. Network models
8 provide insights into how oriens–lacunosum-moleculare and bistratified cell interactions influence
9 the power of local hippocampal CA1 theta oscillations. *Frontiers in systems neuroscience*, 9, 2015.
10 doi: 10.3389/fnsys.2015.00110.
- 11 Ferraguti F., Klausberger T., Cobden P., Baude A., Roberts J., Szucs P., Kinoshita A., Shigemoto R.,
12 Somogyi P., and Dalezios Y. Metabotropic glutamate receptor 8-expressing nerve terminals target
13 subsets of GABAergic neurons in the hippocampus. *J. Neurosci.*, 25(45):10520–10536, 2005. doi:
14 10.1523/JNEUROSCI.2547-05.2005.
- 15 Fries P. Rhythms for cognition: communication through coherence. *Neuron*, 88(1):220–235, 2015. doi:
16 10.1016/j.neuron.2015.09.034.
- 17 Fuentealba P., Begum R., Capogna M., Jinno S., Márton L., Csicsvari J., Thomson A., Somogyi
18 P., and Klausberger T. Ivy cells: a population of nitric-oxide-producing, slow-spiking GABAergic
19 neurons and their involvement in hippocampal network activity. *Neuron*, 57:917–929, 2008. doi:
20 10.1016/j.neuron.2008.01.034.
- 21 Fuentealba P., Klausberger T., Karayannis T., Suen W. Y., Huck J., Tomioka R., Rockland K.,
22 Capogna M., Studer M., Morales M., and Somogyi P. Expression of COUP-TFII nuclear receptor in
23 restricted GABAergic neuronal populations in the adult rat hippocampus. *Journal of Neuroscience*,
24 30:1595–609, 2010. doi: 10.1523/JNEUROSCI.4199-09.2010.

1 Fuhrmann F., Justus D., Sosulina L., Kaneko H., Beutel T., Friedrichs D., Schoch S., Schwarz M. K.,
2 Fuhrmann M., and Remy S. Locomotion, theta oscillations, and the speed-correlated firing of
3 hippocampal neurons are controlled by a medial septal glutamatergic circuit. *Neuron*, 86(5):1253–
4 1264, 2015. doi: 10.1016/j.neuron.2015.05.001.

5 Gasparini S. and Magee J. C. State-dependent dendritic computation in hippocampal CA1 pyramidal
6 neurons. *J. Neurosci.*, 26:2088–2100, 2006. doi: 10.1523/JNEUROSCI.4428-05.2006.

7 Gleeson P., Steuber V., and Silver R. A. neuroConstruct: a tool for modeling networks of neurons in
8 3D space. *Neuron*, 54(2):219–235, 2007. doi: 10.1016/j.neuron.2007.03.025.

9 Goutagny R., Jackson J., and Williams S. Self-generated theta oscillations in the hippocampus. *Nature*
10 *neuroscience*, 12(12):1491—1493, December 2009. ISSN 1097-6256. doi: 10.1038/nm.2440.

11 Gulyas A. I., Toth K., Danos P., and Freund T. Subpopulations of GABAergic neurons containing
12 parvalbumin, calbindin D28k, and cholecystokinin in the rat hippocampus. *J Comp Neurol*, 312:
13 371–378, 1991. doi: 10.1002/cne.903120305.

14 Gulyas A. I., Megias M., Emri Z., and Freund T. F. Total number and ratio of excitatory and
15 inhibitory synapses converging onto single interneurons of different types in the CA1 area of the
16 rat hippocampus. *The Journal of neuroscience*, 19(22):10082–10097, 1999.

17 Hajos N. and Mody I. Synaptic communication among hippocampal interneurons: properties of
18 spontaneous IPSCs in morphologically identified cells. *J. Neurosci.*, 17:8427–8442, 1997.

19 Hasselmo M. E. What is the function of hippocampal theta rhythm?—linking behavioral data to
20 phasic properties of field potential and unit recording data. *Hippocampus*, 15(7):936–949, 2005. doi:
21 10.1002/hipo.20116.

22 Hasselmo M. E., Bodelón C., and Wyble B. P. A proposed function for hippocampal theta rhythm:
23 separate phases of encoding and retrieval enhance reversal of prior learning. *Neural computation*,
24 14(4):793–817, 2002. doi: 10.1162/089976602317318965.

1 Hendrickson P. J., Gene J. Y., Song D., and Berger T. W. Interactions between inhibitory interneurons
2 and excitatory associational circuitry in determining spatio-temporal dynamics of hippocampal
3 dentate granule cells: A large-scale computational study. *Frontiers in systems neuroscience*, 9,
4 2015. doi: 10.3389/fnsys.2015.00155.

5 Hines M. L. and Carnevale N. T. Translating network models to parallel hardware in NEURON.
6 *Journal of neuroscience methods*, 169(2):425–455, 2008. doi: 10.1016/j.jneumeth.2007.09.010.

7 Hines M. L., Eichner H., and Schürmann F. Neuron splitting in compute-bound parallel network
8 simulations enables runtime scaling with twice as many processors. *Journal of computational neu-*
9 *roscience*, 25(1):203–210, 2008a. doi: 10.1007/s10827-007-0073-3.

10 Hines M. L., Markram H., and Schürmann F. Fully implicit parallel simulation of single neurons.
11 *Journal of computational neuroscience*, 25(3):439–448, 2008b. doi: 10.1007/s10827-008-0087-5.

12 Hongo Y., Ogawa K., Takahara Y., Takasu K., Royer S., Hasegawa M., Sakaguchi G., and Ikegaya Y.
13 Topological organization of CA3-to-CA1 excitation. *European Journal of Neuroscience*, 2015. doi:
14 10.1111/ejn.12969.

15 Hu H., Gan J., and Jonas P. Fast-spiking, parvalbumin+ GABAergic interneurons: From cellular
16 design to microcircuit function. *Science*, 345(6196):1255263, 2014. doi: 10.1126/science.1255263.

17 Jedlicka P., Deller T., and Schwarzacher S. W. Computational modeling of GABAA receptor-mediated
18 paired-pulse inhibition in the dentate gyrus. *Journal of computational neuroscience*, 29(3):509–519,
19 2010a. doi: 10.1007/s10827-010-0214-y.

20 Jedlicka P., Hoon M., Papadopoulos T., Vlachos A., Winkels R., Pouloupoulos A., Betz H., Deller T.,
21 Brose N., Varoqueaux F., et al. Increased dentate gyrus excitability in neuroligin-2-deficient mice
22 in vivo. *Cerebral cortex*, page bhq100, 2010b. doi: 10.1093/cercor/bhq100.

23 Jeewajee A., Barry C., Douchamps V., Manson D., Lever C., and Burgess N. Theta phase precession

- 1 of grid and place cell firing in open environments. *Philosophical Transactions of the Royal Society*
2 *of London B: Biological Sciences*, 369(1635):20120532, 2014. doi: 10.1098/rstb.2012.0532.
- 3 Jensen O. and Colgin L. L. Cross-frequency coupling between neuronal oscillations. *Trends in cognitive*
4 *sciences*, 11(7):267–269, 2007. doi: 10.1016/j.tics.2007.05.003.
- 5 Jensen O. and Lisman J. E. Position reconstruction from an ensemble of hippocampal place cells:
6 contribution of theta phase coding. *Journal of neurophysiology*, 83(5):2602–2609, 2000.
- 7 Jinno S., Klausberger T., Marton L. F., Dalezios Y., Roberts J. D. B., Fuentealba P., Bushong E. A.,
8 Henze D., Buzsáki G., and Somogyi P. Neuronal diversity in GABAergic long-range projections
9 from the hippocampus. *J. Neurosci.*, 27:8790–8804, 2007. doi: 10.1523/JNEUROSCI.1847-07.2007.
- 10 Katona L., Lapray D., Viney T. J., Oulhaj A., Borhegyi Z., Micklem B. R., Klausberger T., and
11 Somogyi P. Sleep and movement differentiates actions of two types of somatostatin-expressing
12 GABAergic interneuron in rat hippocampus. *Neuron*, 82(4):872–886, 2014. doi: 10.1016/j.neuron.
13 2014.04.007.
- 14 Kavalali E. T. The mechanisms and functions of spontaneous neurotransmitter release. *Nature Reviews*
15 *Neuroscience*, 16(1):5–16, 2015. doi: 10.1038/nrn3875.
- 16 Kepecs A. and Fishell G. Interneuron cell types are fit to function. *Nature*, 505(7483):318–326, 2014.
17 doi: 10.1038/nature12983.
- 18 Klausberger T. and Somogyi P. Neuronal diversity and temporal dynamics: The unity of hippocampal
19 circuit operations. *Science*, 321:53–57, 2008. doi: 10.1126/science.1149381.
- 20 Klausberger T., Magill P. J., Márton L. F., Roberts J. D. B., Cobden P. M., Buzsáki G., and Somogyi
21 P. Brain-state- and cell-type-specific firing of hippocampal interneurons *in vivo*. *Nature*, 421:
22 844–848, 2003. doi: 10.1038/nature01374.
- 23 Klausberger T., Márton L. F., Baude A., Roberts J. D. B., Magill P. J., and Somogyi P. Spike

1 timing of dendrite-targeting bistratified cells during hippocampal network oscillations *in vivo*. *Nat.*

2 *Neurosci.*, 7:41–47, 2004. doi: 10.1038/nm1159.

3 Klausberger T., Marton L. F., O’Neill J., Huck J. H. J., Dalezios Y., Fuentealba P., Suen W. Y., Papp

4 E., Kaneko T., Watanabe M., Csicsvari J., and Somogyi P. Complementary roles of cholecystokinin-

5 and parvalbumin-expressing GABAergic neurons in hippocampal network oscillations. *J. Neurosci.*,

6 25:9782–9793, 2005. doi: 10.1523/JNEUROSCI.3269-05.2005.

7 Kohl M. M. and Paulsen O. The roles of GABA B receptors in cortical network activity. *Advances in*

8 *pharmacology*, 58:205–229, 2010. doi: 10.1016/S1054-3589(10)58009-8.

9 Kramis R., Vanderwolf C., and Bland B. H. Two types of hippocampal rhythmical slow activity in

10 both the rabbit and the rat: relations to behavior and effects of atropine, diethyl ether, urethane,

11 and pentobarbital. *Experimental neurology*, 49(1):58–85, 1975.

12 Krook-Magnuson E., Luu L., Lee S.-H., Varga C., and Soltesz I. Ivy and neurogliaform interneurons

13 are a major target of μ -opioid receptor modulation. *The Journal of Neuroscience*, 31(42):14861–

14 14870, 2011. doi: 10.1523/JNEUROSCI.2269-11.2011.

15 Lapray D., Lasztozci B., Lagler M., Viney T. J., Katona L., Valenti O., Hartwich K., Borhegyi

16 Z., Somogyi P., and Klausberger T. Behavior-dependent specialization of identified hippocampal

17 interneurons. *Nature neuroscience*, 15(9):1265–1271, 2012. doi: 10.1038/nm.3176.

18 Lee M., Chrobak J., Sik A., Wiley R., and Buzsaki G. Hippocampal theta activity following selective

19 lesion of the septal cholinergic system. *Neuroscience*, 62(4):1033 – 1047, 1994. doi: 10.1016/

20 0306-4522(94)90341-7.

21 Lee S.-H., Foldy C., and Soltesz I. Distinct endocannabinoid control of GABA release at perisomatic

22 and dendritic synapses in the hippocampus. *J. Neurosci.*, 30:7993–8000, 2010. doi: 10.1523/

23 JNEUROSCI.6238-09.2010.

- 1 Lee S.-H., Marchionni I., Bezaire M., Varga C., Danielson N., Lovett-Barron M., Losonczy A., and
2 Soltesz I. Parvalbumin-positive basket cells differentiate among hippocampal pyramidal cells. *Neu-*
3 *ron*, 82(5):1129–1144, 2014. doi: 10.1016/j.neuron.2014.03.034.
- 4 Lisman J. E. and Idiart M. A. Storage of 7 ± 2 short-term memories in oscillatory subcycles. *Science*,
5 267(5203):1512–1515, 1995. doi: 10.1126/science.7878473.
- 6 Lisman J. E. and Jensen O. The theta-gamma neural code. *Neuron*, 77(6):1002–1016, 2013. doi:
7 10.1016/j.neuron.2013.03.007.
- 8 Maccaferri G., David J., Roberts B., Szucs P., Cottingham C. A., and Somogyi P. Cell surface domain
9 specific postsynaptic currents evoked by identified GABAergic neurones in rat hippocampus *in vitro*.
10 *J. Physiol.*, 524:91–116, 2000. doi: 10.1111/j.1469-7793.2000.t01-3-00091.x.
- 11 Maier N., Tejero-Cantero Á., Dorn A. L., Winterer J., Beed P. S., Morris G., Kempter R., Poulet
12 J. F., Leibold C., and Schmitz D. Coherent phasic excitation during hippocampal ripples. *Neuron*,
13 72(1):137–152, 2011. doi: 10.1016/j.neuron.2011.08.016.
- 14 Manns J. R., Zilli E. A., Ong K. C., Hasselmo M. E., and Eichenbaum H. Hippocampal CA1 spiking
15 during encoding and retrieval: relation to theta phase. *Neurobiology of learning and memory*, 87
16 (1):9–20, 2007. doi: 10.1016/j.nlm.2006.05.007.
- 17 Maris E., Fries P., and van Ede F. Diverse phase relations among neuronal rhythms and their potential
18 function. *Trends in neurosciences*, 2016. doi: 10.1016/j.tins.2015.12.004.
- 19 Markram H., Muller E., Ramaswamy S., Reimann M. W., Abdellah M., Sanchez C. A., Ailamaki A.,
20 Alonso-Nanclares L., Antille N., Arsever S., et al. Reconstruction and simulation of neocortical
21 microcircuitry. *Cell*, 163(2):456–492, 2015. doi: 10.1016/j.cell.2015.09.029.
- 22 Megías M., Emri Z., Freund T., and Gulyás A. Total number and distribution of inhibitory and
23 excitatory synapses on hippocampal CA1 pyramidal cells. *Neuroscience*, 102:527–540, 2001. doi:
24 10.1016/S0306-4522(00)00496-6.

- 1 Mercer A., Eastlake K., Trigg H. L., and Thomson A. M. Local circuitry involving parvalbumin-
2 positive basket cells in the CA2 region of the hippocampus. *Hippocampus*, 22(1):43–56, 2012.
- 3 Migliore M., Cannia C., Lytton W. W., Markram H., and Hines M. L. Parallel network simula-
4 tions with neuron. *Journal of computational neuroscience*, 21(2):119–129, 2006. doi: 10.1007/
5 s10827-006-7949-5.
- 6 Mizuseki K., Sirota A., Pastalkova E., and Buzsáki G. Theta oscillations provide temporal windows
7 for local circuit computation in the entorhinal-hippocampal loop. *Neuron*, 64:267–280, 2009.
- 8 Morgan R. J. and Soltesz I. Nonrandom connectivity of the epileptic dentate gyrus predicts a major
9 role for neuronal hubs in seizures. *Proceedings of the National Academy of Sciences*, 105(16):6179–
10 6184, 2008. doi: 10.1073/pnas.0801372105.
- 11 Moser E. I., Kropff E., and Moser M.-B. Place cells, grid cells, and the brain’s spatial representation
12 system. *Annu. Rev. Neurosci.*, 31:69–89, 2008. doi: 10.1146/annurev.neuro.31.061307.090723.
- 13 Neymotin S. A., Lazarewicz M. T., Sherif M., Contreras D., Finkel L. H., and Lytton W. W. Ke-
14 tamine disrupts theta modulation of gamma in a computer model of hippocampus. *The Journal of*
15 *Neuroscience*, 31(32):11733–11743, 2011a. doi: 10.1523/JNEUROSCI.0501-11.2011.
- 16 Neymotin S. A., Lee H., Park E., Fenton A. A., and Lytton W. W. Emergence of physiological
17 oscillation frequencies in a computer model of neocortex. *Frontiers in computational neuroscience*,
18 5, 2011b. doi: 10.3389/fncom.2011.00019.
- 19 Poolos N., Migliore M., and Johnston D. Pharmacological upregulation of h-channels reduces the
20 excitability of pyramidal neuron dendrites. *Nat. Neurosci.*, 5:767–774, 2002. doi: 10.1038/nm891.
- 21 Price C. J., Cauli B., Kovacs E. R., Kulik A., Lambolez B., Shigemoto R., and Capogna M. Neu-
22 rogliaform neurons form a novel inhibitory network in the hippocampal CA1 area. *The Journal of*
23 *neuroscience*, 25(29):6775–6786, 2005. doi: 10.1523/JNEUROSCI.1135-05.2005.

1 Ramaswamy S., Courcol J.-D., Abdellah M., Adaszewski S. R., Antille N., Arsever S., Atenekeng G.,
2 Bilgili A., Brukau Y., Chalimourda A., et al. The neocortical microcircuit collaboration portal: a
3 resource for rat somatosensory cortex. *Frontiers in neural circuits*, 9, 2015. doi: 10.3389/fncir.2015.
4 00044.

5 Remondes M. and Schuman E. M. Role for a cortical input to hippocampal area CA1 in the consoli-
6 dation of a long-term memory. *Nature*, 431(7009):699–703, 2004. doi: 10.1038/nature02965.

7 Robbe D., Montgomery S. M., Thome A., Rueda-Orozco P. E., McNaughton B. L., and Buzsáki
8 G. Cannabinoids reveal importance of spike timing coordination in hippocampal function. *Nature*
9 *neuroscience*, 9(12):1526–1533, 2006. doi: 10.1038/nn1801.

10 Rotstein H. G., Pervouchine D. D., Acker C. D., Gillies M. J., White J. A., Buhl E. H., Whittington
11 M. A., and Kopell N. Slow and fast inhibition and an h-current interact to create a theta rhythm
12 in a model of CA1 interneuron network. *Journal of Neurophysiology*, 94(2):1509–1518, 2005. doi:
13 10.1152/jn.00957.2004.

14 Santhakumar V., Aradi I., and Soltesz I. Role of mossy fiber sprouting and mossy cell loss in hyper-
15 excitability: a network model of the dentate gyrus incorporating cell types and axonal topography.
16 *Journal of neurophysiology*, 93(1):437–453, 2005. doi: 10.1152/jn.00777.2004.

17 Saudargiene A., Cobb S., and Graham B. P. A computational study on plasticity during theta cycles
18 at schaffer collateral synapses on CA1 pyramidal cells in the hippocampus. *Hippocampus*, 25(2):
19 208–218, 2015. doi: 10.1002/hipo.22365.

20 Schneider C. J., Cuntz H., and Soltesz I. Linking macroscopic with microscopic neuroanatomy using
21 synthetic neuronal populations. *PLOS Comput Biol*, 10(10):e1003921, 2014. doi: 10.1371/journal.
22 pcbi.1003921.

23 Schomburg E. W., Anastassiou C. A., Buzsáki G., and Koch C. The spiking component of oscillatory
24 extracellular potentials in the rat hippocampus. *The Journal of Neuroscience*, 32(34):11798–11811,
25 2012. doi: 10.1523/JNEUROSCI.0656-12.2012.

- 1 Schomburg E. W., Fernández-Ruiz A., Mizuseki K., Berényi A., Anastassiou C. A., Koch C., and
2 Buzsáki G. Theta phase segregation of input-specific gamma patterns in entorhinal-hippocampal
3 networks. *Neuron*, 84(2):470–485, 2014. doi: 10.1016/j.neuron.2014.08.051.
- 4 Sejnowski T. J., Koch C., and Churchland P. S. Computational neuroscience. *Science*, 241(4871):
5 1299–1306, 1988. doi: 10.1126/science.3045969.
- 6 Siegle J. H. and Wilson M. A. Enhancement of encoding and retrieval functions through theta phase-
7 specific manipulation of hippocampus. *eLife*, 3:e03061, 2014. doi: 10.7554/eLife.03061.
- 8 Siekmeier P. J. Evidence of multistability in a realistic computer simulation of hippocampus subfield
9 CA1. *Behavioural brain research*, 200(1):220–231, 2009.
- 10 Soltesz I. *Diversity in the Neuronal Machine: Order and Variability in Interneuronal Microcircuits*.
11 Oxford University Press, New York, 2006. doi: 10.1093/acprof:oso/9780195177015.001.1.
- 12 Soltesz I. and Deschenes M. Low-and high-frequency membrane potential oscillations during theta
13 activity in CA1 and CA3 pyramidal neurons of the rat hippocampus under ketamine-xylozine
14 anesthesia. *Journal of neurophysiology*, 70:97–97, 1993.
- 15 Squire L. R. Memory and the hippocampus: a synthesis from findings with rats, monkeys, and
16 humans. *Psychological review*, 99(2):195, 1992. doi: 10.1037/0033-295X.99.2.195.
- 17 Stark E., Eichler R., Roux L., Fujisawa S., Rotstein H. G., and Buzsáki G. Inhibition-induced theta
18 resonance in cortical circuits. *Neuron*, 80(5):1263–1276, 2013. doi: 10.1016/j.neuron.2013.09.033.
- 19 Sterratt D., Graham B., Gillies A., and Willshaw D. *Principles of computational modelling in neuro-*
20 *science*. Cambridge University Press, 2011. doi: 10.1017/CBO9780511975899.
- 21 Szűcs A. Applications of the spike density function in analysis of neuronal firing patterns. *Journal of*
22 *neuroscience methods*, 81(1):159–167, 1998. doi: 10.1016/S0165-0270(98)00033-8.

1 Taxidis J., Mizuseki K., Mason R., and Owen M. R. Influence of slow oscillation on hippocampal
2 activity and ripples through cortico-hippocampal synaptic interactions, analyzed by a cortical-
3 CA3-CA1 network model. *Front Comput Neurosci*, 7, 2013. doi: 10.3389/fncom.2013.00003.

4 Tejada J. and Roque A. C. Computational models of dentate gyrus with epilepsy-induced morpho-
5 logical alterations in granule cells. *Epilepsy & Behavior*, 38:63–70, 2014. doi: 10.1016/j.yebeh.2014.
6 02.007.

7 Thomas E. A., Reid C. A., Berkovic S. F., and Petrou S. Prediction by modeling that epilepsy may be
8 caused by very small functional changes in ion channels. *Archives of neurology*, 66(10):1225–1232,
9 2009. doi: 10.1001/archneurol.2009.219.

10 Thomas E. A., Reid C. A., and Petrou S. Mossy fiber sprouting interacts with sodium channel
11 mutations to increase dentate gyrus excitability. *Epilepsia*, 51(1):136–145, 2010. doi: 10.1111/j.
12 1528-1167.2009.02202.x.

13 Tort A. B., Komorowski R. W., Manns J. R., Kopell N. J., and Eichenbaum H. Theta–gamma coupling
14 increases during the learning of item–context associations. *Proceedings of the National Academy of*
15 *Sciences*, 106(49):20942–20947, 2009. doi: 10.1073/pnas.0911331106.

16 Tricoire L., Pelkey K. A., Erkkila B. E., Jeffries B. W., Yuan X., and McBain C. J. A blueprint for the
17 spatiotemporal origins of mouse hippocampal interneuron diversity. *The Journal of Neuroscience*,
18 31(30):10948–10970, 2011.

19 Tripathy S. J., Savitskaya J., Burton S. D., Urban N. N., and Gerkin R. C. NeuroElectro: a window
20 to the world’s neuron electrophysiology data. *Frontiers in neuroinformatics*, 8, 2014. doi: 10.3389/
21 fninf.2014.00040.

22 Varga C., Golshani P., and Soltesz I. Frequency-invariant temporal ordering of interneuronal discharges
23 during hippocampal oscillations in awake mice. *Proceedings of the National Academy of Sciences*,
24 109(40):E2726–E2734, 2012. doi: 10.1073/pnas.1210929109.

1 Varga C., Oijala M., Lish J., Szabo G. G., Bezaire M., Marchionni I., Golshani P., and Soltesz I.
2 Functional fission of parvalbumin interneuron classes during fast network events. *eLife*, 3:e04006,
3 2014. doi: 10.7554/eLife.04006.

4 Wheeler D. W., White C. M., Rees C. L., Komendantov A. O., Hamilton D. J., and Ascoli G. A.
5 Hippocampome.org: a knowledge base of neuron types in the rodent hippocampus. *eLife*, 4:e09960,
6 2015. doi: 10.7554/eLife.09960.

7 Winkels R., Jedlicka P., Weise F. K., Schultz C., Deller T., and Schwarzacher S. W. Reduced ex-
8 citability in the dentate gyrus network of β iv-spectrin mutant mice in vivo. *Hippocampus*, 19(7):
9 677–686, 2009. doi: 10.1002/hipo.20549.

10 Womelsdorf T., Schoffelen J.-M., Oostenveld R., Singer W., Desimone R., Engel A. K., and Fries P.
11 Modulation of neuronal interactions through neuronal synchronization. *science*, 316(5831):1609–
12 1612, 2007. doi: 10.1126/science.1139597.

13 Ylinen A., Soltész I., Bragin A., Penttonen M., Sik A., and Buzsáki G. Intracellular correlates of
14 hippocampal theta rhythm in identified pyramidal cells, granule cells, and basket cells. *Hippocampus*,
15 5(1):78–90, 1995. doi: 10.1002/hipo.450050110.